REVISION 2

# Celleriite, $(Mn^{2+}_2Al)Al_6(Si_6O_{18})(BO_3)_3(OH)_3(OH)$, a new mineral species of the tourmaline supergroup

FERDINANDO BOSI[1]*, FEDERICO PEZZOTTA[2], ALESSANDRA ALTIERI[1], GIOVANNI B. ANDREOZZI[1], PAOLO BALLIRANO[1], GIOACCHINO TEMPESTA[3], JAN CEMPÍREK[4*], RADEK ŠKODA[4], JAN FILIP[5], RENATA ČOPJAKOVÁ[4], MILAN NOVÁK[4], ANTHONY R. KAMPF[6], EMILY D. SCRIBNER[7], LEE A. GROAT[8] AND R. JAMES EVANS[8]

[1] Department of Earth Sciences, Sapienza University of Rome, Piazzale Aldo Moro, 5, 00185 Rome, Italy
[2] Natural History Museum, Corso Venezia 55, 20121 Milan, Italy
[3] Department of Earth and Geoenvironmental Sciences, University of Bari "Aldo Moro", via Orabona 4, 70125 Bari, Italy
[4] Department of Geological Sciences, Faculty of Science, Masaryk University, 659 37 Brno, Czech Republic
[5] Regional Centre of Advanced Technologies and Materials, Palacký University, Šlechtitelů 27, 783 71 Olomouc, Czech Republic
[6] Mineral Sciences Department, Natural History Museum of Los Angeles County, 900 Exposition Boulevard, Los Angeles, California 90007, USA
[7] Environmental Engineering and Earth Sciences, Clemson University, 445 Brackett Hall, 321 Calhoun Drive, Clemson, South Carolina 29634, USA
[8] Department of Earth, Ocean and Atmospheric Sciences, University of British Columbia, Vancouver, British Columbia V6T 1Z4, Canada

*E-mail: ferdinando.bosi@uniroma1.it; jcemp@sci.muni.cz

## ABSTRACT

Celleriite, $(Mn^{2+}_2Al)Al_6(Si_6O_{18})(BO_3)_3(OH)_3(OH)$, is a new mineral of the tourmaline supergroup. It was discovered in the Rosina pegmatite, San Piero in Campo, Elba Island, Italy (holotype specimen) and in the Pikárec pegmatite, western Moravia, Czech Republic

(co-type specimen). Celleriite in hand specimen is violet to gray-blue (holotype) and dark brownish-green (co-type) with a vitreous luster, conchoidal fracture and white streak. Celleriite has a Mohs hardness of approximately 7, and a calculated density of 3.13 g/cm$^3$ and 3.14 g/cm$^3$ for holotype and its co-type, respectively. In plane-polarized light in thin section, celleriite is pleochroic (O = pale violet and E = light grey-blue in holotype; O = pale green and E = colorless in co-type) and uniaxial negative. Celleriite has trigonal symmetry: space group $R3m$, $Z = 3$, $a = 15.9518(4)$ and $15.9332(3)$ Å, $c = 7.1579(2)$ and $7.13086(15)$ Å, $V = 1577.38(9)$ and $1567.76(6)$ Å$^3$ for holotype and co-type, respectively (data from single-crystal X-ray diffraction). The crystal structure of the holotype specimen was refined to $R1 = 2.89\%$ using 1696 unique reflections collected with Mo$K\alpha$ X-ray intensity data. Structural, chemical and spectroscopic analyses resulted in the formulae:

$^{X}(_{0.58}Na_{0.42})_{\Sigma 1.00}\,^{Y}(Mn^{2+}_{1.39}Fe^{2+}_{0.16}Mg_{0.01}Al_{1.14}Fe^{3+}_{0.01}Li_{0.28}Ti_{0.01})_{\Sigma 3.00}\,^{Z}Al_6$

$[^{T}(Si_{5.99}Al_{0.01})_{\Sigma 6.00}O_{18}](BO_3)_3\,(OH)_3\,^{W}[(OH)_{0.65}F_{0.03}O_{0.32}]_{\Sigma 1.00}$ (for holotype)

and

$^{X}(_{0.51}Na_{0.49})_{\Sigma 1.00}\,^{Y}(Mn^{2+}_{0.90}Fe^{2+}_{0.50}Al_{1.36}Fe^{3+}_{0.04}Li_{0.17}Zn_{0.04})_{\Sigma 3.00}\,^{Z}Al_6\,[^{T}(Si_{5.75}B_{0.25})_{\Sigma 6.00}O_{18}]$

$(BO_3)_3\,(OH)_3\,^{W}[(OH)_{0.35}F_{0.17}O_{0.48}]_{\Sigma 1.00}$ (for co-type).

Celleriite is a hydroxy-species belonging to the *X*-site vacant group of the tourmaline supergroup. The new mineral was approved by the Commission on New Minerals, Nomenclature and Classification of the International Mineralogical Association, proposal n. 2019-089.

In the Rosina pegmatite, celleriite formed an overgrowth at the analogous pole of elbaite–fluor-elbaite–rossmanite crystals during the latest stage of evolution of pegmatite

cavities, after an event of pocket rupture. In the Pikárec pegmatite, celleriite occurs as an intermediate growth sector of elbaite, princivalleite and fluor-elbaite.

**Keywords**: Celleriite, tourmaline, crystal-structure refinement, electron microprobe, Mössbauer spectroscopy, Laser Induced Breakdown Spectroscopy, Laser-Ablation Inductively Coupled Plasma Mass-Spectroscopy, Raman spectroscopy.

## INTRODUCTION

Tourmaline minerals are reported to be the first boron minerals to have formed in Earth's crust and now are the most widespread of minerals for which boron is an essential constituent (Grew et al. 2016; Dutrow and Henry 2018). It is no surprise that this supergroup receives an ever increasing interest from the geoscience community. Tourmaline minerals are complex borosilicates that have been extensively studied in terms of their crystal structure and crystal chemistry (e.g., Foit 1989; Grice and Ercit 1993; Ertl et al. 2002; Novák et al. 2004; Bosi and Lucchesi 2007; Bosi 2013, 2018; Novák et al. 2011; Henry and Dutrow 2011; Henry et al. 2011; Filip et al. 2012; Cempírek et al. 2013; Ertl et al. 2018; Andreozzi et al. 2020).

A general chemical formula of tourmaline can be written as: $XY_3Z_6T_6O_{18}(BO_3)_3V_3W$, where X = Na, K, Ca, □ (= vacancy); Y = Al, Cr, V, $Fe^{3+}$, $Mn^{3+}$, $Fe^{2+}$, Mg, $Mn^{2+}$, Zn, Cu, Li, Ti; Z = Al, Cr, V, $Fe^{3+}$, $Fe^{2+}$, Mg; T = Si, Al, $B^{3+}$; B = $B^{3+}$; V = (OH), O; W = (OH), F and O. Note that the non-italicized letters X, Y, Z, T and B represent groups of cations hosted in the $^{[9]}X$, $^{[6]}Y$, $^{[6]}Z$, $^{[4]}T$ and $^{[3]}B$ crystallographic sites (letters italicized). The letters V and W represent groups of anions accommodated at the

$^{[3]}$O(3) and $^{[3]}$O(1) crystallographic sites, respectively. The H atoms occupy the H(3) and H(1) sites, which are related to O(3) and O(1), respectively. According to the IMA-CNMNC guidelines (Bosi et al. 2019a,b, and references therein): 1) the dominance of a chemical constituent (including vacancies and ion groups with the same valency state) of the dominant-valency state at a given structural site and 2) the principle of valency-imposed double-site occupancy are the compositional criteria recommended to identify tourmalines (Henry et al. 2011). As a result, at least one structural site in a potential new tourmaline has to be dominated by a different chemical constituent from that present at the same site of an existing tourmaline.

Tourmaline-supergroup minerals are currently classified into three groups, *X*-site vacant, alkali and calcic, based on the *X*-site occupancy (Henry et al. 2011). The *X*-site occupancy is usually related to both paragenesis and crystallization conditions of the rock in which tourmaline crystallized, and these relations may be used to reconstruct the host-rock thermal history (Henry and Dutrow 1996; van Hinsberg et al. 2011a,b; Dutrow and Henry 2018; Bosi et al. 2018, 2019c; Ahmadi et al. 2019). A further level of classification into subgroups is based on charge arrangements at the *Y* and *Z* sites. Finally, in accord with the application of the dominant-valency rule, which in turn is followed by the application of the dominant-constituent rule (e.g. Bosi et al. 2019a), the dominant anion at the W position of the general formula allows distinguishing tourmalines into hydroxy-, fluor- and oxy-species (Henry et al. 2011).

A formal description of the new hydroxy-species celleriite is presented here. The mineral is named in honor of Luigi G. Celleri (1828-1900) from San Piero in Campo, Elba Island (Italy), for his contributions to the discovery of several new pegmatites during the second half of the 19$^{th}$ Century. He also gathered hundreds of magnificent specimens

of tourmaline and associated minerals having scientific and collectible interest. Many of these specimens were part of famous Raffaello Foresi and Giorgio Roster collections that today are part of the historic collections of the Mineralogy Museum of the University in Florence (Italy). Luigi G. Celleri also contributed by providing many of the pegmatitic minerals studied by Antonio D'Achiardi (1839-1902) of the University of Pisa (Italy). In 2012, the Mineralogical Museum of San Piero in Campo (Elba Island, Italy) was dedicated to Luigi G. Celleri. The new species and the new name have been approved by the Commission on New Minerals, Nomenclature and Classification (CNMNC) of the International Mineralogical Association (IMA), proposal n. 2019-089 (Bosi et al. 2020a).

Two specimens of celleriite were used to characterize the mineral: 1) the holotype specimen from the type locality Rosina pegmatite, San Piero in Campo, Elba Island (Italy); and 2) a co-type of celleriite from the Pikárec pegmatite, western Moravia (Czech Republic). The holotype was deposited in the collections of the Museo Universitario di Scienze della Terra (MUST), Sapienza University of Rome (Italy), catalogue number 33287/403. Part of holotype specimen, used for measuring the refractive indices, was also deposited in the collections of the Natural History Museum of Milano (Italy), catalogue number M38847. The co-type was deposited in the collection of the Moravian Museum, Brno (Czech Republic), catalogue number A11375, and crystals used for measurement of optical properties are deposited in the collections of the Natural History Museum of Los Angeles County (USA), catalogue number 75055.

## OCCURRENCE, APPEARANCE, PHYSICAL AND OPTICAL PROPERTIES

The holotype specimen (San Piero in Campo, Elba Island, Italy) was discovered in the Rosina pegmatite and occurs as chemically homogeneous, millimeter to sub-

129 millimeter zones within the analogous pole of a zoned tourmaline crystal (Fig. 1).
130 Associated minerals are quartz, albite, K-feldspar, lepidolite, pollucite, petalite,
131 tourmalines (elbaite, fluor-elbaite and rossmanite), beryl, cassiterite, columbite-(Mn),
132 "laumontite", "stilbite" and "heulandite". Its origin is related to miarolitic cavities
133 occurring in the core zone of an asymmetrically zoned LCT-type pegmatite, which is
134 hosted in monzogranite (Pezzotta 2000). San Piero in Campo is also the type locality of
135 two other Mn-dominant tourmalines: tsilaisite and fluor-tsilaisite (Bosi et al. 2005, 2012,
136 2015). The holotype crystal occurs as a growth sector of violet (parallel to the **c**-axis) to
137 gray-blue (perpendicular to the **c**-axis) color that is up to 3 mm in length. This sector is
138 part of a dark colored termination at the analogous pole of a polychrome yellow and green
139 colored tourmaline crystal that is 15 mm long (Fig. 2).

140 The co-type specimen (western Moravia, Czech Republic) was discovered in an
141 elbaite-subtype granitic pegmatite in Pikárec (e.g., Zahradníček 2012). At this locality,
142 celleriite occurs as part of a dark brownish-green crystal (color of the hand specimen)
143 rimmed by pink tourmaline from the root of a pegmatite pocket; the crystal is ca. 3 cm
144 long and 1.5 cm wide. Celleriite is associated with albite (variety cleavelandite), quartz,
145 K-feldspar and other tourmaline-supergroup minerals: elbaite, fluor-elbaite and
146 princivalleite [$Na(Mn^{2+}_2Al)Al_6(Si_6O_{18})(BO_3)_3(OH)_3O$; Bosi et al. 2020b]. It formed by
147 fractional crystallization from B-rich residual albitic liquid in the final stage of the
148 pegmatite magmatic crystallization. The pegmatite is a member of the Stráž̌ek pegmatite
149 field (Novák and Cempírek 2010) in the central part of the Stráž̌ek Moldanubicum in the
150 Moldanubian Zone of the Bohemian Massif. The pegmatite is associated with numerous
151 other barren pocket pegmatites with smoky quartz and black tourmaline (Gadas et al.
152 2012), and several fractionated pegmatites that belong to the elbaite or lepidolite subtypes

of the complex-type, rare-element class of granitic pegmatites (after Černý et al. 2012). The co-type crystal occurs as zones that are 2–5 mm wide and brownish-green to green in color, in a Mn-rich elbaite and princivalleite crystal, which can be distinguished only by chemical analysis. Celleriite is visually indistinguishable from the zones of tourmaline with the other composition. Other parts of the same crystal (termination and crystal core) are blue or violet and their composition is oxy-schorl to foitite. Fluor-elbaite that rims the darker core is pale pink in thin section.

Celleriite has a vitreous luster, white streak and no fluorescence. Its Mohs hardness is approximately 7. It is brittle with a conchoidal fracture, as inferred from the holotype crystal. Its calculated density, on the basis of the empirical formula and unit-cell volume refined from single-crystal X-ray diffraction data, is 3.13 g/cm$^3$ (holotype) and 3.14 g/cm$^3$ (co-type). Celleriite is transparent in thin section and pleochroic with O = pale violet and E = pale grey-blue (holotype) and O = pale green and E = colorless (co-type) in transmitted light. Celleriite is uniaxial negative with refractive indices as follows: for the holotype, $\omega$ = 1.643(1) and $\varepsilon$ = 1.628(1) measured with a refractometer, and for the co-type, $\omega$ = 1.656(2) and $\varepsilon$ = 1.627(2) measured with a spindle stage; white LED light (approximately 5.500 K) was used for optical determinations in both cases. The mean index of refraction, density and chemical composition lead to excellent compatibility indexes (Mandarino 1981) for the holotype (1 – *K*p/*K*c = 0.038) and its co-type (1 – *K*p/*K*c = 0.036).

## EXPERIMENTAL METHODS AND RESULTS

### General comment

For the Italian celleriite holotype specimen, crystal Structure REFinement (SREF), Electron MicroProbe (EMP) and μ-Laser Induced Breakdown Spectroscopy (μ-LIBS) data were all obtained from the same crystal fragment (black square in Fig. 2a). Complementary Mössbauer Spectroscopy data (MS), refractive indices and powder X-Ray Diffraction (XRD) data were acquired from a larger portion of the chemically zoned tourmaline crystal.

For the Czech co-type of celleriite, the crystal used for the SREF was extracted, using a microdrill-equipped microscope, from a domain previously examined using EMP and Raman spectroscopy, and just next to a Laser-Ablation Inductively Coupled Plasma Mass Spectroscopy (LA-ICP-MS) analytical spot. The Mössbauer spectrum and powder XRD pattern were obtained from a larger domain from the same compositional zone.

**Single-crystal structure refinement**

**Holotype.** A representative fragment crystal of celleriite from the Rosina pegmatite (San Piero in Campo, Elba Island, Italy) was selected for XRD measurements on a Bruker KAPPA APEX-II single-crystal diffractometer (Sapienza University of Rome, Earth Sciences Department), equipped with a charge-coupled device (CCD) area detector (6.2 × 6.2 cm active detection area, 512 × 512 pixels) and a graphite-crystal monochromator using Mo*K*α radiation from a fine-focus sealed X-ray tube. The sample-to-detector distance was 4 cm. A total of 2453 exposures (step = 0.2°, time/step = 20 s) covering a full reciprocal sphere with a redundancy of approximately 13 was collected. The intensity data were processed and corrected for Lorentz, polarization and background effects using the APEX2 software program of Bruker AXS. The data were corrected for

absorption using a multi-scan method (SADABS). No violation of *R*3*m* symmetry was detected.

Structure refinement was done using the SHELXL-2013 program (Sheldrick 2015). Starting coordinates were taken from Bosi et al. (2015). Variable parameters were scale factor, extinction coefficient, atom coordinates, site-scattering values (for *X, Y* and *Z* sites) and atomic-displacement factors. Attempts to refine the extinction coefficient yielded values within its standard uncertainty, thus it was not refined. Neutral scattering factors were used for the cations and oxygen atoms. As for the atomic model refinement, the *X* site was modeled using the Na scattering factor. The *Y* site was refined by setting the Li occupancy to 0.28 atoms per formula unit (apfu) and allowing the remainder of the site to refine as Mn = (2.72 – Al) apfu. The *Z* site was modelled by Al versus Mn. The *T*, *B* and anion sites were modeled with Si, B and O scattering factors, respectively, and with a fixed occupancy of 1 since refinement with unconstrained occupancies showed no significant deviations from this value. There were no correlations greater than 0.7 between the parameters at the end of the refinement.

**Co-type**. A selected single-crystal of celleriite from Pikárec pegmatite (Moravia, Czech Republic) was studied using a Rigaku HighFlux HomeLab diffractometer (Masaryk University in Brno, CEITEC X-ray Diffraction and Bio-SAXS Core Facility) equipped with rotating anode X-ray source (multilayered optics, Mo*K*α radiation), partial χ axis goniometer and CCD detector (Saturn 724+ HG). The sample-to-detector distance was 3 cm. A total of 2048 exposures (step = 0.25°, time/step = 4 or 8 s) was collected with CrystalClear software and processed with CrysAlisPro. The structures were solved and refined using SHELX-2013 software package (Sheldrick 2015). Starting coordinates were taken from Cempírek et al. (2013). Variable parameters were scale factor, atom

coordinates, site-scattering values (for *X, Y, Z* and *T* sites) and atomic-displacement factors. The *X* site was modeled using the Na scattering factor. The *Y* site was refined by setting the Li occupancy to 0.17 apfu and allowing the remainder of the site to refine as Mn = (2.83 – Al) apfu. The *Z* and *T* sites were modelled by Al versus Mn and Si versus B, respectively. The *B* and anion sites were modeled with B and O scattering factors, respectively, and with a fixed occupancy of 1. The O(1) site was modelled with occupancy of O and F fixed to the value of the structural formula (see below). There were no correlations greater than 0.72 between the parameters at the end of the refinement.

For the holotype specimen and its co-type, Table 1 shows selected bond lengths and a CIF with all structural data is deposited.

**X-ray powder diffraction**

**Holotype.** X-ray powder diffraction data were collected with a focusing-beam (Göbel mirror) Bruker AXS D8 Advance operating in transmission in θ-θ geometry. The instrument was fitted with a PSD VÅntec-1 with the acceptance angle set to 6° 2θ. The goniometer had a 250 mm radius. Data were measured using Cu*K*α radiation from a fine-focus sealed X-ray tube (Table 2). Unit cell parameters refined using the Rietveld method from the powder data are as follows: $a$ = 15.9330(2) Å, $c$ = 7.13593(9) Å and $V$ = 1568.82(4) Å$^3$.

**Co-type**. The phase composition and structural data of pulverized tourmaline were determined by powder XRD with an X`Pert PRO diffractometer (Malvern Panalytical, Ltd) operating in Bragg-Brentano geometry with goniometer radius 240 mm. The diffractometer was equipped with an iron-filtered Co*K*α radiation source, programmable divergence and diffracted beam anti-scatter slits, and a fast PIXcel detector. The XRD

pattern was measured in the 2θ range from 5 to 105° and the data were processed using HighScore Plus software in conjunction with PDF-4+ and ICSD databases (Table 3). Unit cell parameters refined using the Rietveld method from the powder data are as follows: $a$ = 15.9344(3) Å, $c$ = 7.1313(2) Å and $V$ = 1568.08(6) Å$^3$.

**Electron microprobe analysis**

**Holotype**. The crystal used for the SREF was analyzed with a Cameca SX50 electron microprobe with wavelength dispersive spectrometers (WDS mode) at the Istituto di Geologia Ambientale e Geoingegneria (Rome, Italy), CNR. The analytical conditions were: accelerating voltage 15 kV, beam current 15 nA, spot diameter 10 μm. Minerals and synthetic compounds were used as standards: wollastonite (Si, Ca), magnetite (Fe), rutile (Ti), corundum (Al), vanadinite (V), fluorphlogopite (F), periclase (Mg), jadeite (Na), orthoclase (K), sphalerite (Zn), rhodonite (Mn), metallic Cr and Cu. The PAP routine was applied (Pouchou and Pichoir, 1991). The results (Table 4) represent mean values of 10 spot analyses. Vanadium, Cr, Cu, Zn, Ca and K were below detection limits (< 0.03 wt%).

**Co-type.** The crystal used for the SREF was analyzed with a Cameca SX-100 electron microprobe (WDS mode) at Masaryk University in Brno, Czech Republic. The analytical conditions were: accelerating voltage 15 kV, beam current 10 nA, spot diameter 5 μm. Minerals and synthetic compounds were used as standards: sanidine (Si, Al), titanite (Ti), almandine (Fe), spessartine (Mn), gahnite (Zn), albite (Na), topaz (F). The X-Phi matrix correction was applied (Merlet 1994). Chemical analysis is shown in the Table 4; no other elements heavier than F were detected.

## Mössbauer spectroscopy

**Holotype**. Crystal fragments extracted from the Italian celleriite-rich portion of the zoned tourmaline were powdered to prepare a Mössbauer absorber containing 20 mg of tourmaline, which was loaded in a Plexiglas sample holder with diameter of 2 mm. Measurements were performed using a spectrometer with a $^{57}$Co point source of 0.37 GBq (10 mCi) embedded in a Rh matrix. The spectrum was collected within 8 days in transmission mode at room temperature and at velocity between –4 to +4 mm/s, and was recorded in a multichannel analyzer with 512 channels. The velocity was calibrated with a 25-μm thick α-Fe foil. The obtained spectrum was fitted to Lorentzian line-shapes using the RECOIL 1.04 fitting program. The final fitting model consisted of four absorption doublets, three for $^{[6]}Fe^{2+}$ and one for $^{[6]}Fe^{3+}$, with hyperfine parameters (Table 5) consistent with those optimized by Andreozzi et al. (2008). The $Fe^{2+}/Fe_{Tot}$ and $Fe^{3+}/Fe_{Tot}$ ratios are quantified at 0.96(3) and 0.04(3), respectively (Fig. 3a).

**Co-type.** Tourmaline fragments extracted from the cut sample were studied using transmission $^{57}$Fe Mössbauer spectroscopy on tourmaline at the Regional Centre of Advanced Technologies and Materials, Palacký University, Olomouc, Czech Republic. The spectrum of a powdered tourmaline sample (ground under acetone) was accumulated in a constant acceleration mode using a $^{57}$Co in Rh source and 1024 channel detector at room temperature. The isomer shift was calibrated relative to an α-Fe foil. The spectrum was folded and fitted by Lorentz functions using the computer program CONFIT2000 (Žák and Jirásková 2006). The resulting five absorption doublets (Fig. 3b) indicate very low amounts of $Fe^{3+}$, quantified at 0.05(3) $Fe^{3+}/Fe_{Tot}$ ratio (Table 5).

## Micro-Laser Induced Breakdown Spectroscopy

For the holotype specimen, Li analysis was performed using 110 mJ of energy per pulse by double pulse Q-Switched (Nd-YAG, $\lambda$ = 1064 nm) laser with a 1 μs delay between the two pulses. The small spot size (7-10 μm) was obtained using a petrographic optical microscope (objective lens 10X NA 0.25 WD 14.75 mm). The LIBS spectra were acquired by AvaSpec Fiber Optic Spectrometer (390–900 nm with 0.3 nm resolution) with a delay of 2 μs after the second pulse and were integrated for 1 ms. Quantitative data were obtained by generating a linear regression using the main Li emission line intensity (670.706 nm corresponding to resonance transition $1s^2\ 2s > 1s^2\ 2p$), which is particularly sensitive to Li amounts. The linear fit was made using spectra recorded on two NIST standard glasses (SRM 610 and 612) and three Li-bearing tourmaline samples from Filip et al. (2012), Grew et al. (2018) and Bosi et al. (2019d). The result corresponds to 0.42 wt% of $Li_2O$ (Table 4).

**Laser-Ablation Inductively Coupled Plasma Mass-Spectroscopy**

For the co-type of celleriite, Li analysis was performed using a LA-ICP-MS at the Department of Chemistry, Masaryk University, Brno. It consists of a UP 213 (New Wave Research, Inc., Fremont, CA, USA) laser-ablation system and an Agilent 7500 CE (Agilent Technologies, Santa Clara, CA, USA) ICPMS spectrometer. A commercial Q-switched Nd:YAG laser ablation device works at the fifth harmonic frequency, which corresponds to the wavelength of 213 nm. Laser ablation was performed with laser spots of diameter 40 μm, laser fluence 3 J/cm$^2$, and repetition rate 10 Hz. Lithium and trace element contents were calculated using NIST SRM 610 and 612 standards and Si and Al (values from earlier EMP analysis from measured spots) were used as internal reference

318 elements after baseline correction and integration of the peak area. The result corresponds
319 to 0.26 wt% of $Li_2O$ (Table 4).
320
321 **Raman spectroscopy**
322 The Raman spectrum of the co-type of celleriite was obtained from a thin section
323 using a Horiba Labram HR Evolution spectrometer. This dispersive, edge-filter-based
324 system was equipped with an Olympus BX 41 optical microscope, a diffraction grating
325 with 600 grooves per mm, and a Peltier-cooled, Si-based CCD detector. After careful
326 tests with different lasers (473, 532 and 633 nm), the 532 nm diode laser with the beam
327 power of 20 mW at the sample surface was selected for spectra acquisition to minimize
328 analytical artefacts. The Raman signal was collected in the range of 100–4000 $cm^{-1}$ with a
329 100x objective (NA 0.9). The system was operated in the confocal mode with a beam
330 diameter of ~1 μm. No visual damage to the analyzed surface was observed at these
331 conditions after the excitation. Raman shift calibration was done using the Rayleigh line
332 and low-pressure Ne-discharge lamp emissions. The wavenumber accuracy was ~0.5 $cm^{-1}$
333 and the spectral resolution was ~2 $cm^{-1}$. Band fitting was completed after appropriate
334 background correction, assuming combined Lorentzian-Gaussian band shapes using
335 Voight function. Based on the equation of Kutzschbach et al. (2016), the broad band at
336 3365 $cm^{-1}$ indicates presence of at least 0.11 apfu $^{[4]}B$ (Fig. 4); the actual amount may be
337 higher due to partial deviation of the crystal from the ideal direction perpendicular to **c**.
338
339 **Determination of atomic fractions**
340 In accordance with the structural data, the $B^{3+}$ content was assumed to be
341 stoichiometric (B = 3.00 apfu). The Fe oxidation state was determined by MS. All Mn

342 was considered to be $Mn^{2+}$ based on the MS results and Fe and Mn redox potential
343 arguments. Lithium was determined by μ-LIBS (holotype) and LA-ICP-MS (co-type).
344 The (OH) content and the formula were then calculated by charge balance with the
345 assumption (T + Y + Z) = 15.00 apfu and 31 anions. The very good agreement between
346 the number of electrons per formula unit (epfu) derived from EMP and SREF analysis
347 (236.8 epfu vs. 235.8 epfu for the holotype sample, and 236.0 epfu vs. 236.5 epfu for the
348 cotype sample) supports the stoichiometric assumptions.
349
350 **Determination of site population and mineral formula**
351 The anion site populations in the studied samples follow the general preference
352 suggested for tourmaline (e.g., Henry et al. 2011): the O(3) site (V position in the general
353 formula) is occupied by $(OH)^{-}$, while the O(1) site (W position in the general formula)
354 can be occupied by $O^{2-}$, $(OH)^{-}$ and $F^{-}$. The *T* site is occupied by Si and Al (for the
355 holotype specimen) or $B^{3+}$ (for the co-type specimen). The latter is supported by Raman
356 spectroscopy (Fig. 4). The cation distribution over the *Y* and *Z* sites has been optimized
357 according to the procedure of Bosi et al. (2017) and the ionic radii of Bosi (2018). More
358 specifically, the site distribution of Al, $Fe^{3+}$, $Mn^{2+}$ and $Fe^{2+}$ was obtained by minimizing
359 the residuals between the calculated and observed structural data [such as bond distance,
360 bond valence, site scattering expressed in terms of mean atomic number (m.a.n.)] by
361 using a least-square program. Lithium and the minor amounts of Ti and Zn were fixed at
362 the *Y* site, whereas the minor amount of Mg was fixed at *Z*. The resulting empirical
363 crystal-chemical formulae for the studied samples are as follows:
364 $^{X}(_{0.58}Na_{0.42})_{\Sigma 1.00}{}^{Y}(Mn^{2+}_{1.10}Fe^{2+}_{0.16}Al_{1.45}Fe^{3+}_{0.01}Li_{0.28}Ti_{0.01})_{\Sigma 3.00}{}^{Z}(Al_{5.70}Mn^{2+}_{0.29}Mg_{0.01})_{\Sigma 6.00}$
365 $[^{T}(Si_{5.99}Al_{0.01})_{\Sigma 6.00}O_{18}](BO_3)_3(OH)_3{}^{W}[(OH)_{0.65}F_{0.03}O_{0.32}]_{\Sigma 1.00}$ (holotype)

366

367 $^{X}(_{0.51}Na_{0.49})_{\Sigma 1.00}\,^{Y}(Mn^{2+}_{0.81}Fe^{2+}_{0.50}Zn^{2+}_{0.04}Al_{1.46}Fe^{3+}_{0.04}Li_{0.17})_{\Sigma 3.00}\,^{Z}(Al_{5.91}Mn^{2+}_{0.09})_{\Sigma 6.00}$

368 $[^{T}(Si_{5.75}B_{0.25})_{\Sigma 6.00}O_{18}]\,(BO_3)_3\,(OH)_3\,^{W}[(OH)_{0.35}F_{0.17}O_{0.48}]_{\Sigma 1.00}$ (co-type)

369 The observed data and those calculated from the optimized site populations are in
370 excellent agreement (Table 6). The robustness of these site populations was confirmed by
371 another optimization procedure (Wright et al. 2000), which led to very similar results. Of
372 particular interest is the refined *Z*-site occupancy value of the holotype specimen (CIF and
373 Table 6). It is consistent with the occurrence of minor amounts of cations (up to 0.3 apfu),
374 such as Mn, with atomic numbers larger than Al: *Z*-m.a.n. = 13.47(8) is in fact
375 significantly larger than the expected value for a *Z* site fully occupied by Al (*Z*-m.a.n. =
376 13). The latter is corroborated by the refined <*Z*-O> value (1.919 Å), which reflects the
377 presence of cations larger than Al, such as Mn, when compared to the typical <*Z*-O>
378 values observed for a *Z* site fully occupied by Al (1.902-1.913 Å; Bosi and Andreozzi
379 2013). Table 7 (on deposit) reports the weighted bond-valences.

380

381 ## CLASSIFICATION, END-MEMBER FORMULA AND RELATION TO OTHER

382 ## SPECIES

383 For classification purposes, the previously reported site allocation of ions has to be
384 recast in an ordered formula with the *Z* site fully occupied by Al (Henry et al. 2011) to
385 overcome the issues of uncertainty associated with cation order-disorder across *Y* and *Z*:

386 $^{X}(_{0.58}Na_{0.42})_{\Sigma 1.00}\,^{Y}(Mn^{2+}_{1.39}Fe^{2+}_{0.16}Mg_{0.01}Al_{1.14}Fe^{3+}_{0.01}Li_{0.28}Ti_{0.01})_{\Sigma 3.00}\,^{Z}Al_6$

387 $[^{T}(Si_{5.99}Al_{0.01})_{\Sigma 6.00}\,O_{18}]\,(BO_3)_3\,(OH)_3\,^{W}[(OH)_{0.65}F_{0.03}O_{0.32}]_{\Sigma 1.00}$ (holotype)

This is the peer-reviewed, final accepted version for American Mineralogist, published by the Mineralogical Society of America.
The published version is subject to change. Cite as Authors (Year) Title. American Mineralogist, in press.
DOI: https://doi.org/10.2138/am-2021-7818. http://www.minsocam.org/

388 $^{X}(_{0.51}Na_{0.49})_{\Sigma 1.00}\,^{Y}(Mn^{2+}_{0.90}Fe^{2+}_{0.50}Zn^{2+}_{0.04}Al_{1.36}Fe^{3+}_{0.04}Li_{0.17})_{\Sigma 3.00}\,^{Z}Al_6$

389 $[^{T}(Si_{5.75}B_{0.25})_{\Sigma 6.00}O_{18}]\,(BO_3)_3\,(OH)_3\,^{W}[(OH)_{0.35}F_{0.17}O_{0.48}]_{\Sigma 1.00}$ (co-type)

390 These compositions are consistent with a tourmaline belonging to *X*-site vacant group,
391 subgroup 1 (Henry et al. 2011): it is vacancy-dominant at the X position of the general
392 formula of tourmaline $XY_3Z_6T_6O_{18}(BO_3)_3V_3W$ and hydroxy-dominant at W with
393 $(OH+F)^- > O^{2-}$ and (OH) >> F . Aluminum is the dominant cation at the *Z* site, whereas
394 the valency-imposed double site-occupancy for the *Y* site is required to obtain a charge-
395 balanced end-member composition. In this regard, we can consider the IMA-CNMNC
396 rules (Bosi et al. 2019a,b) and explore the resulting two possible end-member charge
397 arrangements consistent with the composition:

398 $^{X}0\,^{Y}(2^{+}_{2}3^{+})\,^{Z}3^{+}_{6}\,(^{T}4^{+}_{6}2^{-}_{18})\,(^{B}3^{+}2^{-}_{3})_3\,^{O(3)}1^{-}_{3}\,^{O(1)}1^{-}$

399 $^{X}0\,^{Y}(3^{+}_{2}1^{+})\,^{Z}3^{+}_{6}\,(^{T}4^{+}_{6}2^{-}_{18})\,(^{B}3^{+}2^{-}_{3})_3\,^{O(3)}1^{-}_{3}\,^{O(1)}1^{-}$

400 where O(3) ≡ V and O(1) ≡ W. The replacement of most formal charges with the
401 corresponding dominant constituents at the sites leads to:

402 $^{X}\;^{Y}(2^{+}_{2}3^{+})\,^{Z}Al_6\,(^{T}Si_6O_{18})\,(^{B}BO_3)_3\,^{O(3)}(OH)_3\,^{O(1)}(OH)$

403 $^{X}\;^{Y}(3^{+}_{2}1^{+})\,^{Z}Al_6\,(^{T}Si_6O_{18})\,(^{B}BO_3)_3\,^{O(3)}(OH)_3\,^{O(1)}(OH)$

404 Of particular interest is the site-total-charge at the *Y* sites (= +7), which suggests two
405 possible charge and atomic arrangements compatible with +7 and the chemical
406 composition for the holotype specimen:

407 $^{Y}(2^{+}_{2}3^{+})^{\Sigma 7+} \rightarrow {}^{Y}(2^{+}_{2}3^{+})_{0.78} \rightarrow {}^{Y}(2^{2+}_{1.56}Al^{3+}_{0.78})$ = 2.34 apfu (limited by $2^+$ contents);

408 $^{Y}(3^{+}_{2}1^{+})^{\Sigma 7+} \rightarrow {}^{Y}(3^{+}_{2}1^{+})_{0.28} \rightarrow {}^{Y}(Al^{3+}_{0.56}Li^{+}_{0.28})$ = 0.85 apfu (limited by Li contents).

409 As a result, and in accordance with the dominant-valency rule, the proportion of the
410 arrangement $^{Y}(2^{+}_{1.56}Al^{3+}_{0.78})$ is greater than the proportion of $^{Y}(Al^{3+}_{0.56}Li^{+}_{0.28})$. In
411 accordance with the dominant-constituent rule, $Mn^{2+}$ prevails among the divalent cations

This is the peer-reviewed, final accepted version for American Mineralogist, published by the Mineralogical Society of America.
The published version is subject to change. Cite as Authors (Year) Title. American Mineralogist, in press.
DOI: https://doi.org/10.2138/am-2021-7818. http://www.minsocam.org/

412 (1.39 $Mn^{2+}$ apfu > 0.10 $Fe^{2+}$ > 0.01 $Mg^{2+}$). Thus, the atomic arrangement $^{Y}(Mn^{2+}{}_2Al)$ is
413 the dominant one in the holotype specimen from Rosina pegmatite, San Piero in Campo,
414 Elba Island (Italy): $^{Y}(Mn^{2+}{}_2Al)_{0.695}$ = 2.09 apfu, corresponding to ca. 70% of the site
415 occupancy. Similar arguments apply to the co-type of celleriite form Pikárec pegmatite,
416 western Moravia (Czech Republic): as the proportion of the charge arrangement
417 $^{Y}(2^{+}{}_2 3^{+})_{0.70}$ = 2.10 apfu is larger than the proportion of $^{Y}(3^{+}{}_2 1^{+})_{0.17}$ = 0.51 apfu and $Mn^{2+}$ >
418 $Fe^{2+}$ > $Zn^{2+}$, the dominant atomic arrangement is $^{Y}(Mn^{2+}{}_2Al)_{0.45}$ (= 1.35 apfu). Therefore,
419 $Mn^{2+}$ is dominant at the *Y* site and the end-member composition can be represented as
420 $(Mn^{2+}{}_2Al)Al_6(Si_6O_{18})(BO_3)_3(OH)_3(OH)$, which also requires Al at the *Y* site for charge-
421 balance reasons (valency-imposed double-site occupancy). Since no tourmalines have yet
422 been proposed with this end-member composition, the studied tourmalines can be
423 classified as a new species with the name celleriite. In the vacant-subgroup 1 (Henry et al.
424 2011), celleriite is related to foitite and magnesio-foitite by the homovalent substitutions
425 $Mn^{2+} \leftrightarrow Fe^{2+}$ and $Mn^{2+} \leftrightarrow Mg^{2+}$, respectively; properties of the three tourmalines are
426 compared in Table 8. The heterovalent substitution $2Mn^{2+} \leftrightarrow Al^{3+} + Li^{+}$ relates celleriite
427 to rossmanite (Fig. 5).
428

429 ## GEOLOGICAL AND FORMATION ENVIRONMENT OF CELLERIITE

430 **Holotype**. Celleriite on Elba Island occurs in the Rosina pegmatite, which is
431 located a few hundred meters south of the San Piero in Campo village, close to several
432 other historic pegmatitic mineral localities such as “Prado”, “Masso Foresi”, “Fonte del
433 Prete” and “Facciatoia” (Orlandi and Pezzotta 1996). These above-mentioned historic
434 localities were mined during the 19$^{th}$ Century, whereas the Rosina pegmatite was
435 discovered on private land by one of the authors (FP) in early 1990 and only started to be

436 mined for collectibles and for specimens suitable for use in scientific research in 1992.
437 From 2013 to 2016, the locality was included in a Research Permit of industrial purposes
438 for Li and Rb mineralization in the pegmatite field that occurs along the eastern border
439 zone of the Monte Capanne pluton in west Elba. At present, part of the Rosina pegmatite
440 is still in place and the locality is included in the didactic field visits organized by the
441 Mineralogy Museum "Luigi Celleri" (MUM) of San Piero in Campo. The Rosina
442 pegmatite is hosted in porphyritic monzogranite at the eastern border of the
443 monzogranitic Mount Capanne pluton (7.4-6.9 Ma; Barboni et al. 2015). The pegmatite
444 has a complex shape, trends roughly N-S and has a variable dip angle of 40–75° W. The
445 major productive section of the body is approximately 14 m long and is 0.6–2.1 m wide.
446 The shallowest portions of the pegmatite body are the widest ones and are characterized
447 by mostly aplitic textures with minor coarse-grained pegmatitic lenses. At greater depths,
448 the body becomes more pegmatitic and divides into two major veins that are
449 interconnected by a number of small veinlets. The Rosina pegmatite belongs to the LCT
450 family, is strongly miarolitic with cavities > 1 m in length and is significantly asymmetric
451 in terms of its textures, mineralogy and geochemistry. Textural asymmetries are evident
452 in the pegmatitic portions: the axial core-miarolitic zone, which is rich in lepidolite,
453 petalite and pollucite, divides the body into a medium-grained lower section enriched in
454 albite with minor K-feldspar, plus quartz, spessartine and tourmaline in comb texture,
455 together with patches of sekaninaite and an upper coarse-grained section enriched in K-
456 feldspar with minor albite, quartz and tourmaline. This is evidenced by the composition of
457 tourmaline as well as the occurrence of other geochemically evolved minerals such as
458 petalite and pollucite. Cavities found at shallower levels contain mostly dark-colored
459 tourmaline (from schorl to Fe-rich elbaite with variable Mn-contents to foitite) together

with pale-blue beryl (aquamarine variety) and spessartine. Cavities found at deeper levels contain abundant polychrome and rose tourmaline, pink beryl (morganite variety), petalite and pollucite.

Celleriite was found in a relatively large tabular cavity (ca. $100 \times 70 \times 25$ cm) that occurs in an intermediate zone of the body. This cavity was discovered during mining performed in 2008. It displays the typical asymmetric distribution of the minerals: the roof is mostly covered by K-feldspar crystals, with quartz, minor albite and petalite, rare tourmaline crystals and a number of pink beryl crystals, while the floor is rich in albite, petalite, quartz and drusy tourmalines, with locally abundant pollucite. Tourmaline crystals grew in the cavity in the direction of the analogous pole, ranging in length from approximately 1–3 cm with a diameter of up to 1 cm. The crystals are olive-green to yellow-green in color and are all characterized by a darker purplish-bluish-gray termination. Chemical analyses revealed an elbaite to fluor-elbaite composition along the crystal and mostly celleriite composition at the termination. The source crystal of celleriite shows compositional zoning from celleriite to Mn-rich, $Fe^{2+}$-bearing elbaite, fluor-elbaite and scarce rossmanite (Fig. 2a,b)

**Co-type**. The elbaite-subtype pegmatite from Pikárec near Křižanov, situated ~1.5 km S of the village, forms NW-SE-trending subvertical dike ca. 3 m thick and 50–70 m long, cutting amphibolite. From the contact inwards, the pegmatite consists of the following units (zones): (i) thin, coarse-grained (~1–2 cm) outer granitic unit (Plg+Kfs+Qz+Bt±Tur) that evolves gradually into volumetrically dominant (ii) medium- to coarse-grained (0.5 to 3 cm) graphic unit (Kfs+Qz > Ab+Qz). It locally contains biotite in its outermost parts where graphic textures are poorly developed. Very abundant black tourmaline is present in several morphological types in this unit; it is locally associated

with Grt+Qz graphic intergrowths. The graphic unit evolves to masses of (iii) pale brown to orange blocky K-feldspar (up to 10 cm) closely associated with or replaced by (iv) bluish, medium-grained albite (albite unit), and (v) small masses of quartz in the central part of the dike. Small (vi) pockets, up to 1–2 $dm^3$ in size, are spatially associated with the units (iii), (iv) and (v); the pockets (vi) are lined with crystals of K-feldspar, smoky quartz, albite and polychrome Li-bearing tourmaline.

Along with major (Kfs, Plg, Ab, Qz), minor (Tur, Bt) and common accessory (Grt, Ap, löllingite) pegmatite constituents, several rare accessory minerals [columbite-(Mn), tantalite-(Mn), cassiterite, microlite, zircon, pollucite] were identified within the albite unit (Zahradníček 2012; Zahradníček and Novák 2012). Rare equidimensional grains of colorless to pinkish beryl, up to 1 cm in size, occur in albite that is close to pockets. Garnet is present as two textural and compositional types: graphic intergrowths of Qz+Grt ($Sps_{85-68}$ $Alm_{15-31}$ $Grs_{0-1}$) up to 3 cm in size in the inner part of graphic unit, and very rare subhedral orange-red grains of spessartine ($Sps_{89-91}$ $Alm_{9-11}$), up to 1 cm in size, in albite close to the pockets. Very rare small flakes of polylithionite and muscovite were found in pockets, the former also exceptionally in albite (Zahradníček and Novák 2012).

Tourmaline is present in a variety of morphological and paragenetic types. Rare, black prismatic crystals and their aggregates, up to 3 cm in size, occur in the outermost parts of the graphic unit. Black tourmaline in graphic (pseudographic) intergrowths with quartz is by far the most abundant morphology forming at least ~90 % by volume of tourmaline in the pegmatite body. Aggregates of these intergrowths can reach up 15 cm in length, whereas the diameter of the individual tourmaline grains in the intergrowths varies from ~1–10 mm. The Qz+Tur intergrowths typically contain a larger tourmaline crystal in the center; they coarsen towards the pegmatite core and may evolve to large conical

508 crystals of black tourmaline up to 3 cm long. The conical crystals occur in the innermost
509 part of the graphic unit and blocky feldspar, at the contact with the albite unit and
510 pockets, and are locally rimmed by pink tourmaline. The pockets contain short prismatic
511 crystals of zoned tourmaline (greenish black to deep red to pink) that are up to 5 cm long
512 and commonly rooted at the top of the conical black crystals mentioned above. The last
513 tourmaline generation in the pockets occurs as aggregates of small, prismatic pink crystals
514 (up to 3 mm long) that overgrow crystals of K-feldspar and albite. Other color varieties of
515 tourmaline (green, blue) common in Li-bearing granitic pegmatites (e.g., Jolliff et al.
516 1986; Novák and Povondra 1995; Selway et al. 1999) are absent. Celleriite in the Pikárec
517 pegmatite forms a transitional zone in the dark brownish-green core of tourmaline from
518 the root of a pegmatite pocket. The source crystal of celleriite shows compositional
519 zoning from celleriite to elbaite, princivalleite and fluor-elbaite (Fig. 2c).
520

521 **Petrogenesis of celleriite**

522 At the type specimen locality (Rosina pegmatite, Elba Island, Italy), paragenetic
523 observations of the cavity provide evidence that the celleriite overgrew the analogous
524 termination of tourmaline crystals during the latest stages of the cavity evolution, after an
525 episode of rigid mechanical shock and fracturing of the cavity. This caused some crystals
526 in the cavity, including some tourmalines, to break and formed thin fractures in the
527 pegmatite around the cavity. Subsequently, celleriite grew not only at the analogous pole
528 at the termination of the tourmaline crystals, but also on top of the broken bases with an
529 identical composition and pattern of chemical variation.

530 Manganese enrichment in late-stage pocket tourmaline is a characteristic feature
531 of elbaite-subtype pegmatites (e.g., Novák and Povondra 1995; Novotný et al. 2019), in

addition to their strongly peraluminous (Galliski et al. 2012) or transitional varieties (e.g., Dixon et al. 2014; Čopjaková et al. 2015). The main distinction from the otherwise similar Mn-enrichment in lepidolite-subtype pegmatites is the lower content of fluxing elements such as F and $P_2O_5$ in the elbaite-subtype pegmatites. As a result, there is little lepidolite and Mn-rich apatite that would deplete the albitic melt in Mn. This is accompanied by relatively low F content in elbaite-subtype pegmatites that typically remains below 0.5 apfu in tourmaline until the hydrothermal-metasomatic stage of pegmatite crystallization, which is characterized by fluor-elbaite to fluor-liddicoatite compositions (e.g., Novotný et al. 2019; Zahradníček 2012; Flégr 2016). Interestingly, it seems that the presence of common spessartine-almandine garnet in magmatic pegmatite units does not preclude high Mn-enrichment in late-stage primary tourmaline in pegmatite pockets (Zahradníček 2012; Flégr 2016; Novotný 2020). This conclusion is consistent with the study of Haralampiev and Grover (1993) in which the high partitioning of Mn into garnet was suggested preventing the development of tsilaisite. In the case of the Elba Island pegmatites, spessartine garnet generally stored most of the Mn present in the pegmatitic melt and crystallized in core zones at a relatively early stage of geochemical evolution. In the pegmatite portions in which the cavities are characterized by a relatively low geochemical evolution (as evidenced by the occurrence of dark and Fe-rich tourmalines, pale blue beryl and a lack of pollucite), spessartine crystallized as a late-stage mineral, forming well-shaped crystals on previously crystallized minerals such as quartz, feldspars, schorl and beryl. Conversely, in the pegmatite portions where the degree of geochemical evolution of the core zone is very advanced (as evidenced by polychrome and pink tourmaline, the beryl variety morganite, abundant petalite, pollucite and lepidolite), spessartine occurs crystallized early, inside feldspars and quartz, and

556 sparsely as a rim of crystals around the pocket. As for the highly geochemically evolved
557 Elba Island pegmatites, in the relatively rare cases when spessartine is absent, tourmaline
558 incorporates most of the Mn that was present in the pegmatitic melt. Its crystals display a
559 strong Mn enrichment, reaching the compositions of tsilaisite and fluor-tsilaisite. When
560 both spessartine and tourmaline are present, the Mn enrichment in tourmaline is not
561 enough to achieve tsilaisite and fluor-tsilaisite compositions, but a late-stage tourmaline
562 can form with strong Mn enrichment and reaching celleriite composition.

563 In the specific case of the Rosina pegmatite, spessartine is relatively abundant and
564 tourmaline is not particularly enriched in Mn (MnO up to ~6 wt. % in elbaite and fluor-
565 elbaite). Nevertheless, in the pocket in which celleriite was discovered, a strong Mn
566 enrichment occurred at the termination of the tourmaline crystals, in a growth sector that
567 formed after a pocket rupture. Such a pocket rupture is evidenced by: i) the formation of
568 thin fractures penetrating from the cavity into the surrounding solid pegmatite; ii) partial
569 collapse of quartz and feldspar crystal aggregates in the cavity; and iii) the rupture of
570 some of the tourmaline crystals. An event such as this could be related to some brittle
571 deformation due to tensional stress associated with, for instance, thermal contraction
572 during cooling of the rock. It is associated with significant albitization of K-feldspar,
573 corrosion of spessartine and alteration of the few tapering crystals of biotite to white
574 mica. Fracturing was followed by a recrystallization event, with overgrowth of quartz and
575 feldspar crystals and the formation of significant dark overgrowths (mostly composed of
576 celleriite) at the analogous poles of tourmaline crystals, both on the pedion faces of
577 terminated crystals and the fracture surfaces of broken crystals. These phenomena of
578 corrosion, alteration and crystallization may be ascribed to the aggressive late-stage fluids
579 from pegmatite pockets, which penetrated into the fractures and, because some B was still

present, allowed for the formation of a late-stage tourmaline generation. A similar feature was noted in the Cruzeiro pegmatite with the development of fibrous tourmaline by Dutrow and Henry (2000). An additional piece of evidence for the occurrence of a late-stage enrichment of Mn in the cavities of Elba pegmatites, and, for instance, the Rosina pegmatite, is documented by the local crystallization of helvite (Pezzotta 2000).

Dark–terminations at the analogous pole of multicolored tourmaline crystals are quite characteristic for tourmalines of Elba Island pegmatites and are typically $Fe^{2+}$-rich (e.g., Orlandi and Pezzotta 1996). Although there is little documentation in the literature, the formation of such late-stage overgrowths in Elba tourmalines is likely due to partial re-opening of the geochemical system and the introduction of Fe, and possible minor quantities of other elements such as Mg and Ti, which were incorporated in earlier crystallized minerals. This new system is related to the hydrothermal alteration of these earlier crystallized minerals such as biotite and sekaninaite. Systematic analyses of the dark terminations in Elba tourmalines indicate mostly foitite and rarely schorl composition (Pezzotta et al. 1996; Altieri 2019). In the case of the celleriite-bearing pocket, the relative abundance of spessartine in the surrounding solid pegmatite coupled with the scarcity of biotite and other Fe-rich minerals may account for a Mn-rich, Fe-poor source in the late-stage fluids. The latter was responsible for the crystallization of a relatively dark tourmaline overgrowth composed of celleriite in the Rosina pegmatite, instead of the typical occurrence of foitite.

At the co-type specimen locality (Pikárec pegmatite, Czech Republic), a gradual, moderate increase of Mn and Al followed by a much more pronounced decrease of Fe at low F and Na levels seems to be a primary feature that is unrelated to the hydrothermal stage. The hydrothermal stage is characterized by fluor-elbaite composition with high F,

Na and Al, and very low Fe and Mn (Fig. 2b; see also Zahradníček 2012). Therefore, locally extreme Mn content in the pegmatite albite zone combined with low F and $P_2O_5$ contents seem to be the most significant factors controlling the formation of celleriite in the Pikárec pegmatite.

## IMPLICATIONS

The formation of Mn-dominant tourmalines (celleriite, tsilaisite and fluor-tsilaisite) requires specific geochemical conditions that are rare in nature. According to Simmons et al. (2011), the original pegmatite-forming melt (preferably a B-rich peraluminous melt) must be relatively low in Fe and enriched in Mn and B; moreover, during the early stages of crystallization, Fe must be removed, but abundant B and Mn must still be available when tourmaline crystallizes. In this regard, the occurrence of the new mineral celleriite provides an excellent example of a mineral species formed under unusual environmental conditions. Thus, celleriite appears to be valuable in understanding Earth as a complex, evolving system in which metasomatic fluid-rock interactions may lead to new mineral-forming environments, in particular for B minerals (Hazen and Ausubel 2016; Grew et al. 2016). Moreover, the crystal overgrowth of celleriite implies that while the dark termination—the so-called *Moor's head* textural type—is characteristic for the Elba Island pegmatites, it is not a feature exclusively produced by Fe enrichment, but may also imply the presence of a Mn-dominant component.

## ACKNOWLEDGMENTS

Chemical analyses were completed with the kind assistance of M. Serracino, to whom the authors express their gratitude. The Associate Editor, E.S. Grew, the Technical Editor and the reviewers, P. Bačík and D.J. Henry, are thanked for their constructive comments. Funding by Sapienza University of Rome (Prog. Università 2018 to F. Bosi) and DeepCarbon Observatory (2016 to G.B. Andreozzi) are gratefully acknowledged. JC, RŠ, RČ and MN acknowledge support from the project GAČR 17-17276S. The research was supported by an NSERC Discovery Grant to LAG (funding reference 06434). Support from the John Jago Trelawney Endowment to the Mineral Sciences Department of the Natural History Museum of Los Angeles County to ARK is acknowledged. Part of the data presented in this paper were obtained at CEITEC, Core Facility X-ray Diffraction and Bio-SAXS supported by MEYS CR (LM2018127).

639 **REFERENCES CITED**

640 Ahmadi, S., Tahmasbi, Z., Khalaji, A.A., and Zal, F. (2019) Chemical variations and
641 origin of tourmalines in laleh zar granite of Kerman (Southeast Iran). Periodico di
642 Mineralogia, 88, 117–129.

643 Altieri, A. (2019) Evoluzione cristallochimica di tormaline delle pegmatiti a gemme
644 dell'Isola d'Elba. Master Thesis, Sapienza University of Rome, 129 p. (in Italian).

645 Andreozzi, G.B., Bosi, F., and Longo, M. (2008) Linking Mössbauer and structural
646 parameters in elbaite-schorl-dravite tourmalines. American Mineralogist, 93, 658–
647 666.

648 Andreozzi, G.B., Bosi, F., Celata, B., Capizzi, L.S., Stagno, V., and Beckett-Brown, C.
649 (2020) Crystal-chemical behavior of $Fe^{2+}$ in tourmaline dictated by structural
650 stability: insights from a schorl with formula
651 $Na^{Y}(Fe^{2+}{}_2Al)^{Z}(Al_5Fe^{2+})(Si_6O_{18})(BO_3)_3(OH)_3(OH,F)$ from Seagull batholith (Yukon
652 Territory, Canada). Physics and Chemistry of Minerals, 47, 25.

653 Barboni, M., Annen, C., and Schoene, B. (2015) Evaluating the construction and the
654 evolution of upper crustal magma reservoirs with coupled U/Pb zircon
655 geochronology and thermal modeling: a case study from the Mt. Capanne pluton
656 (Elba, Italy). Earth and Planetary Science Letters, 432, 436–448,

657 Bosi, F. (2013) Bond-valence constraints around the O1 site of tourmaline. Mineralogical
658 Magazine, 77, 343–351.

659 Bosi, F. (2014) Bond valence at mixed occupancy sites. I. Regular polyhedra. Acta
660 Crystallographica, B70, 864–870.

661 Bosi, F. (2018) Tourmaline crystal chemistry. American Mineralogist, 103, 298–306.

662 Bosi, F., and Lucchesi, S. (2007) Crystal chemical relationships in the tourmaline group:
663 structural constraints on chemical variability. American Mineralogist, 92, 1054–
664 1063.
665 Bosi, F., Agrosì, G., Lucchesi, S., Melchiorre G., and Scandale, E. (2005) Mn-tourmaline
666 from island of Elba (Italy). Crystal chemistry. American Mineralogist, 90, 1661–
667 1668
668 Bosi, F., Skogby, H., Agrosì, G., and Scandale, E. (2012) Tsilaisite,
669 $NaMn_3Al_6(Si_6O_{18})(BO_3)_3(OH)_3OH$, a new mineral species of the tourmaline
670 supergroup from Grotta d'Oggi, San Pietro in Campo, island of Elba, Italy.
671 American Mineralogist, 97, 989–994.
672 Bosi, F., and Andreozzi, G.B. (2013) A critical comment on Ertl et al. (2012): "Limita-
673 tions of $Fe^{2+}$ and $Mn^{2+}$ site occupancy in tourmaline: Evidence from $Fe^{2+}$- and
674 $Mn^{2+}$-rich tourmaline. American Mineralogist, 98, 2183–2192.
675 Bosi, F., Andreozzi, G.B., Agrosì, G., and Scandale, E. (2015) Fluor-tsilaisite,
676 $NaMn_3Al_6(Si_6O_{18})(BO_3)_3(OH)_3F$, a new tourmaline from San Piero in Campo (Elba,
677 Italy) and new data on tsilaisitic tourmaline from the holotype specimen locality.
678 Mineralogical Magazine, 79, 89–101.
679 Bosi, F., Reznitskii, L., Hålenius, U., and Skogby, H. (2017) Crystal chemistry of Al–V–
680 Cr oxy-tourmalines from Sludyanka complex, Lake Baikal, Russia. European
681 Journal of Mineralogy, 29, 457–472.
682 Bosi, F., Naitza, S., Skogby, H., Secchi, F., Conte, A.M., Cuccuru, S., Hålenius, U., De
683 La Rosa, N., Kristiansson, P., Charlotta Nilsson, E.J., Ros, L., and Andreozzi, G.B.
684 (2018) Late magmatic controls on the origin of schorlitic and foititic tourmalines

685 from late-Variscan peraluminous granites of the Arbus pluton (SW Sardinia, Italy):
686 Crystal-chemical study and petrological constraints. Lithos, 308–309, 395–411.
687 Bosi, F., Hatert, F., Hålenius, U., Pasero, M., Miyawaki, R., and Mills, S.J. (2019a) On
688 the application of the IMA-CNMNC dominant-valency rule to complex mineral
689 compositions. Mineralogical Magazine, 83, 627–632.
690 Bosi, F., Biagioni, C., and Oberti, R. (2019b) On the chemical identification and
691 classification of minerals. Minerals, 9, 591.
692 Bosi, F., Naitza, S., Secchi, F., Conte, A.M., Cuccuru, S., Andreozzi, G.B., Skogby, H.,
693 and Hålenius, U. (2019c) Petrogenetic controls on the origin of tourmalinite veins
694 from Mandrolisai igneous massif (Central Sardinia, Italy): Insights from tourmaline
695 crystal chemistry. Lithos, 342–343, 333–344.
696 Bosi, F., Skogby, H., and Hålenius, U. (2019d) Thermally induced cation redistribution in
697 fluor-elbaite and Fe-bearing tourmalines. Physics and Chemistry of Minerals, 46,
698 371–383.
699 Bosi, F., Pezzotta, F., Altieri, A., Andreozzi, G. B., Ballirano, P., and Tempesta, G.
700 (2020a) Celleriite, IMA 2019-089. CNMNC Newsletter No. 53, February 2020,
701 page 211. European Journal of Mineralogy, 32, 209–213.
702 Bosi, F., Pezzotta, F., Skobgy, H., Altieri, A., Hålenius, U., Tempesta, G. and Cempírek,
703 J. (2020b) Princivalleite, IMA 2020-056. CNMNC Newsletter No. 58, December
704 2020, European Journal of Mineralogy, 32 (in press).
705 Brese, N.E., and O'Keeffe, M. (1991) Bond-Valence Parameters for Solids. Acta
706 Crystallographica, B47, 192–197.
707 Cempírek, J., Houzar, S., Novák, M., Groat, L.A., Selway, J.B., and Šrein, V. (2013)
708 Crystal structure and compositional evolution of vanadium-rich oxy-dravite from

graphite quartzite at Bítovánky, Czech Republic. Journal of Geosciences, 58, 149–162.

Černý, P., London, D., Novák, M. (2012) Granitic pegmatites as reflection of their sources. Elements, 8, 289–294

Čopjaková, R., Škoda, R., Vašinová-Galiová, M., Novák, M., and Cempírek, J. (2015) Sc- and REE-rich tourmaline replaced by Sc-rich REE-bearing epidote-group mineral from the mixed (NYF+LCT) Kracovice pegmatite (Moldanubian Zone, Czech Republic). American Mineralogist, 100, 1434–1451.

Dixon, A., Cempírek, J., and Groat, L.A. (2014) Mineralogy and geochemistry of pegmatites on Mount Begbie, British Columbia. Canadian Mineralogist, 52, 129–164.

Dutrow, B.L., and Henry, D.J. (2000) Complexly zoned fibrous tourmaline, Cruzeiro mine, Minas Gerais, Brazil: A record of evolving magmatic and hydrothermal fluids: Canadian Mineralogist, 38, 131–143.

Dutrow, B.L., and Henry, D.J. (2018) Tourmaline compositions and textures: reflections of the fluid phase. Journal of Geosciences, 63, 99–110.

Ertl, A., Hughes, J.M., Pertlik, F., Foit, F.F. Jr., Wright, S.E., Brandstatter, F., and Marler, B. (2002) Polyhedron distortions in tourmaline. Canadian Mineralogist, 40, 153–162.

Ertl, A., Henry, D.J., and Tillmanns, E. (2018) Tetrahedral substitutions in tourmaline: a review. European Journal of Mineralogy, 30, 465–470.

Filip, J., Bosi, F., Novák, M., Skogby, H., Tuček, J., Čuda, J., and Wildner, M. (2012) Redox processes of iron in the tourmaline structure: example of the high-

732 temperature treatment of Fe3+-rich schorl. Geochimica et Cosmochimica Acta, 86,
733 239–256.
734 Flégr, T. (2016) Vývoj chemického složení turmalínů z elbaitového pegmatitu Řečice.
735 MS thesis, Faculty of Science, Masaryk University, Brno (in Czech).
736 Foit, F.F. Jr. (1989) Crystal chemistry of alkali-deficient schorl and tourmaline structural
737 relationships. American Mineralogist, 74, 422–431.
738 Gadas, P., Novák, M., Staněk, J., Filip, J., and Vašinová Galiová, M. (2012)
739 Compositional evolution of zoned tourmaline crystals from pockets in common
740 pegmatites, the Moldanubian Zone, Czech Republic. Canadian Mineralogist, 50,
741 895–912.
742 Gagné, O.C., and Hawthorne, F.C. (2015) Comprehensive derivation of bond-valence
743 parameters for ion pairs involving oxygen. Acta Crystallographica, B71, 562–578.
744 Galliski, M.A., Márquez-Zavalía, M.F., Lira, R., Cempírek, J., and Škoda, R. (2012)
745 Mineralogy and origin of the dumortierite-bearing pegmatites of Virorco, San Luis,
746 Argentina. Canadian Mineralogist, 50, 873–894.
747 Grice, J.D., and Ercit, T.S. (1993) Ordering of Fe and Mg in the tourmaline crystal
748 structure: the correct formula. Neues Jahrbuch für Mineralogie, Abhandlungen, 165,
749 245–266.
750 Grew, E.S., Krivovichev, S.V., Hazen, R.M., and Hystad, G. (2016) Evolution of
751 structural complexity in boron minerals. Canadian Mineralogist, 54, 125–143.
752 Grew, E.S., Bosi, F., Gunter, M., Hålenius, U., Trumbull, R.B., and Yates, M.G. (2018)
753 Fluor-elbaite, lepidolite and Ta-Nb oxides from a pegmatite of the 3000 MA Sinceni
754 pluton, Swaziland: Evidence for lithium-cesium-tantalum (LCT) pegmatites in the
755 Mesoarchean. European Journal of Mineralogy, 30, 205–218.

Haralampiev, A.G. and Grover, J. (1993) Synthesis experiments in the binary system tsilaisite–dravite, $Na(Mn_xMg_{1-x})_3Al_6(BO_3)_3Si_6O_{18}(OH)_4$, at T = 375-700° and P = 2000 bars; does garnet control the occurrence of tourmaline? Geological Society of America Abstracts with Program, 25, 94–55.

Hawthorne, F.C., Selway, J.B., Kato, A., Matsubara, S., Shimizu, M., Grice, J.D., and Vajdak, J. (1999) Magnesiofoitite, $(Mg_2Al)Al_6(Si_6O_{18})(BO_3)_3(OH)_4$, a new alkali-deficient tourmaline. Canadian Mineralogist, 37, 1439–1443.

Hazen, R.M., and Ausebel, J. (2016) On the nature and significance of rarity in mineralogy. American Mineralogist, 101, 1245–1251.

Henry, D.J., and Dutrow, B.L. (1996) Metamorphic tourmaline and its petrologic applications. In: Grew, E.S., Anvitz, L.M. (Eds.), Boron: Mineralogy, Petrology and Geochemistry, Reviews in Mineralogy and Geochemistry. vol. 33. Chantilly, Virginia, pp. 503–557 Mineralogical Society of America.

Henry, D.J., and Dutrow, B.L. (2011) The incorporation of fluorine in tourmaline: Internal crystallographic controls or external environmental influences? Canadian Mineralogist, 49, 41–56.

Henry, D.J., Novák, M., Hawthorne, F.C., Ertl, A., Dutrow, B., Uher, P., and Pezzotta, F. (2011) Nomenclature of the tourmaline-supergroup minerals. American Mineralogist, 96, 895–913.

Jolliff, B.L., Papike, J.J., and Shearer, C.K. (1986) Tourmaline as a recorder of pegmatite evolu- tion: Bob Ingersoll Pegmatite, Black Hills, South Dakota. American Mineralogist, 71, 472–500.

Kutzschbach, M., Wunder, B., Rhede, D., Koch-Müller, M., Ertl, A., Giester, G., Heinrich, W., and Franz, G. (2016) Tetrahedral boron in natural and synthetic

780 HP/UHP tourmaline: evidence from Raman spectroscopy, EMPA, and single-crystal
781 XRD. American Mineralogist, 101, 93–104.
782 Mandarino, J.A. (1981) The Gladstone-Dale relationship. Part IV: the compatibility
783 concept and its application. Canadian Mineralogist, 19, 441–450.
784 MacDonald, D.J., Hawthorne, F.C., and Grice, J.D. (1993) Foitite,
785 $(Al,Fe^{3+})Al_6Si_6O_{18}(BO_3)_3(OH)_4$, a new alkali-deficient tourmaline: description and
786 crystal structure. American Mineralogist, 78, 1299–1303.
787 Merlet C. (1994) An Accurate Computer Correction Program for Quantitative Electron
788 Probe Microanalysis, Microchimica Acta, 114, 363–376.
789 Novák, M., and Cempírek, J., (eds) (2010) Granitic pegmatites and mineralogical
790 museums in Czech Republic. IMA 2010 Field Trip Guide CZ2. Acta Mineralogica
791 Petrographica Field Guide Series 6, Szeged, pp 1–56.
792 Novák, M., and Povondra, P. (1995) Elbaite pegmatites in the Moldanubicum: a new
793 subtype of the rare-element class. Mineralogy and Petrology, 55, 159–176.
794 Novák, M., Povondra, P., and Selway, J.B. (2004) Schorl-oxy-schorl to dravite-
795 oxydravite tourmaline from granitic pegmatites; examples from the Moldanubicum,
796 Czech Republic. European Journal of Mineralogy, 16, 323–333.
797 Novák, M., Škoda, P., Filip, J., Macek, I., and Vaculovič, T. (2011) Compositional trends
798 in tourmaline from intragranitic NYF pegmatites of the Třebíč Pluton, Czech
799 Republic; electron microprobe, Mössbauer and LA-ICP-MS study. Canadian
800 Mineralogist, 49, 359–380.
801 Novotný, F. (2020) Mineralogy of the Dolní Rožínka elbaite-subtype pegmatite. MS
802 thesis, Faculty of Science, Masaryk University, Brno (in Czech).

803 Novotný, F., Novák, M., and Cempírek, J. (2019) Chemical composition of tourmaline
804 from the Dolní Rožínka elbaite pegmatite. Bulletin of Mineralogy and Petrology,
805 27, 38–45.
806 Orlandi, P., and Pezzotta, F. (1996) Minerali dell'Isola d'Elba, i minerali dei giacimenti
807 metalliferi dell'Elba orientale e delle pegmatiti del Monte Capanne. Ed. Novecento
808 Grafico, Bergamo. 248 pp (in Italian).
809 Pezzotta, F. (2000) Internal structures, parageneses and classification of the miarolitic
810 (Li-bearing) complex pegmatites of Elba Island (Italy). Mineralogy and petrology of
811 shallow depth pegmatites. Papers from the First International Workshop. Memorie
812 della Società Italiana di Scienze Naturali e del Museo Civico di Storia Naturale di
813 Milano, 30, 29–43.
814 Pezzotta, F., Hawthorne, F., Cooper, M.A., and Teerstra, D., (1996) Fibrous foitite from
815 S. Piero in Campo, Elba, Italy. Canadian Mineralogist, 34, 741–744.
816 Pouchou, J.L., and Pichoir, F. (1991) Quantitative analysis of homogeneous or stratified
817 microvolumes applying the model "PAP." In K.F.J. Heinrich and D.E. Newbury,
818 Eds., Electron Probe Quantitation, p. 31–75. Plenum, New York.
819 Selway, J.B., Novák, M., Černý, P., and Hawthorne, F.C. (1999) Compositional evolution
820 of tourmaline in lepidolite-subtype pegmatites. European Journal of Mineralogy, 11,
821 569–584.
822 Sheldrick, G.M. (2015) Crystal structure refinement with SHELXL. Acta
823 Crystallographica, C71, 3–8.
824 Simmons, W.B., Falster, A.U., and Laurs, B.M. (2011) A survey of Mn-rich yellow
825 tourmaline from worldwide localities and implications for the petrogenesis of the
826 granitic pegmatites. Canadian Mineralogist, 49, 301–319.

van Hinsberg, V.J., Henry, D.J., and Marschall, H.R. (2011a) Tourmaline: an ideal indicator of its host environment. Canadian Mineralogist, 49, 1–16.

van Hinsberg, V.J., Henry, D.J., and Dutrow, B.L. (2011b) Tourmaline as a petrologic forensic mineral: a unique recorder of its geologic past. Elements, 7, 327–332.

Wright, S.E., Foley, J.A., and Hughes, J.M. (2000) Optimization of site occupancies in minerals using quadratic programming. American Mineralogist, 85, 524–531.

Zahradníček, L. (2012) Vývoj textur a chemického složení zonálních turmalínů z elbaitového pegmatitu v Pikárci u Křižanova. MS thesis, Faculty of Science, Masaryk University, Brno (in Czech).

Zahradníček, L., and Novák, M. (2012) Lithium-bearing micas from elbaite-subtype pegmatites in the Western Moravia, Czech Republic. Acta Musei Moraviae, Scientiae geologicae, 97, 25–37. In Czech with English summary.

Žák, T., and Jirásková, Y. (2006) CONFIT: Mössbauer spectra fitting program. Surface and Interface Analysis, 38, 710–714.

## List of tables

**Table 1.** Selected bond lengths (Å) for celleriite from the Rosina pegmatite, San Piero in Campo, Elba Island, Italy (holotype) and the Pikárec pegmatite, western Moravia, Czech Republic (co-type).

**Table 2.** X-ray powder diffraction data (*d* in Å) for celleriite from the Rosina pegmatite, San Piero in Campo, Elba Island, Italy (holotype). Whenever a single box is reported for the $I/I_0$ of a group of nearby reflections, the asterisk, if present, indicates the most intense one(s).

**Table 3.** X-ray powder diffraction data ($d$ in Å) for celleriite from the Pikárec pegmatite, western Moravia, Czech Republic (co-type). Only reflections with $I_{meas} \geq 2$ are reported.

**Table 4.** Chemical composition for celleriite from the Rosina pegmatite, San Piero in Campo, Elba Island, Italy (holotype) and the Pikárec pegmatite, western Moravia, Czech Republic (co-type).

**Table 5.** Room-temperature Mössbauer parameters for celleriite from Italy from the Rosina pegmatite, San Piero in Campo, Elba Island, Italy (holotype) and the Pikárec pegmatite, western Moravia, Czech Republic (co-type).

**Table 6.** Optimized cation site populations (apfu), mean atomic numbers and mean bond lengths (Å) from Italy obtained at room-temperature from the Rosina pegmatite, San Piero in Campo, Elba Island, Italy (holotype) and the Pikárec pegmatite, western Moravia, Czech Republic (co-type).

**Table 7 (on deposit).** Weighted bond valences (valence units) for celleriite from the Rosina pegmatite, San Piero in Campo, Elba Island, Italy (holotype) and from the Pikárec pegmatite, western Moravia, Czech Republic (co-type).

**Table 8.** Comparative data for the holotype specimens of celleriite, foitite and magnesio-foitite.

## List of figures and figure captions

**Figure 1**. Dark celleriite overgrowth on the termination of an elbaitic crystal (1.7 cm tall) from the Rosina pegmatite (San Piero in Campo, Elba Island, Italy), with

873 albite and quartz. One spessartine crystal is visible at the lower left of the
874 specimen grown inside the quartz-albite aggregate. Photo by F. Picciani.

875 **Figure 2**. Zoning of tourmaline crystals containing celleriite from the Rosina pegmatite,
876 San Piero in Campo, Elba Island, Italy (a,b; holotype specimen) along the **c**-
877 axis, and the Pikárec pegmatite, western Moravia, Czech Republic (c; co-type
878 specimen). Core to rim along the **c**-axis for: (a) Holotype specimen with
879 celleriite zones within the analogous pole of a chemically zoned tourmaline
880 crystal (the black square identifies the crystal fragment extracted for the
881 SREF); (b) compositional zoning of the holotype specimen, and (c) the co-
882 type specimen. Abbreviations: Elb = elbaite, F-Elb = fluor-elbaite, Clr =
883 celleriite, Ros = rossmanite, Prn = princivalleite.

884 **Figure 3.** Room temperature $^{57}$Fe Mössbauer spectrum for celleriite; (a) the holotype
885 specimen from the Rosina pegmatite, San Piero in Campo, Elba Island (Italy);
886 (b) the co-type specimen from the Pikárec pegmatite, western Moravia, Czech
887 Republic.

888 **Figure 4.** Raman spectrum for the co-type celleriite specimen from the Pikárec pegmatite,
889 western Moravia, Czech Republic.

890 **Figure 5**. Dominant occupancy of the *Y* site with the *Z* site = Al in *X*-site vacant group
891 tourmaline. Plot of celleriite compositions on the $Fe^{2+}$-$Mn^{2+}$-2Li diagram. The
892 holotype specimen is from the Rosina pegmatite, San Piero in Campo, Elba
893 Island, Italy; the co-type of celleriite is from the Pikárec pegmatite, western
894 Moravia, Czech Republic.

This is the peer-reviewed, final accepted version for American Mineralogist, published by the Mineralogical Society of America.
The published version is subject to change. Cite as Authors (Year) Title. American Mineralogist, in press.
DOI: https://doi.org/10.2138/am-2021-7818. http://www.minsocam.org/

**TABLE 1**. Selected bond lengths (Å) for celleriite from the Rosina pegmatite, San Piero in Campo, Elba Island, Italy (holotype) and the Pikárec pegmatite, western Moravia, Czech Republic (co-type)

| Sample | holotype | co-type |
|---|---|---|
| *X*-O(2) × 3 | 2.519(7) | 2.534(3) |
| *X*-O(5) × 3 | 2.773(4) | 2.7576(18) |
| *X*-O(4) × 3 | 2.837(5) | 2.8151(19) |
| <*X*-O> | 2.710 | 2.702 |
| *Y*-O(2) × 2 | 1.971(2) | 1.9714(9) |
| *Y*-O(1) | 2.023(3) | 2.0114(16) |
| *Y*-O(6) × 2 | 2.041(2) | 2.0311(9) |
| *Y*-O(3) | 2.134(3) | 2.1390(16) |
| <*Y*-O> | 2.030 | 2.026 |
| *Z*-O(6) | 1.874(2) | 1.8648(9) |
| *Z*-O(8) | 1.8857(19) | 1.8823(9) |
| *Z*-O(7) | 1.8866(19) | 1.8771(8) |
| *Z*-O(8)’ | 1.924(2) | 1.9171(9) |
| *Z*-O(7)’ | 1.9641(19) | 1.9530(8) |
| *Z*-O(3) | 1.9774(15) | 1.9767(7) |
| <*Z*-O> | 1.919 | 1.912 |
| *B*-O(2) | 1.360(5) | 1.355(2) |
| *B*-O(8) × 2 | 1.380(3) | 1.3823(12) |
| <*B*-O> | 1.373 | 1.373 |
| *T*-O(6) | 1.607(2) | 1.6097(9) |
| *T*-O(7) | 1.6097(17) | 1.6143(8) |
| *T*-O(4) | 1.6209(10) | 1.6217(5) |
| *T*-O(5) | 1.6356(12) | 1.6342(6) |
| <*T*-O> | 1.618 | 1.620 |

This is the peer-reviewed, final accepted version for American Mineralogist, published by the Mineralogical Society of America.
The published version is subject to change. Cite as Authors (Year) Title. American Mineralogist, in press.
DOI: https://doi.org/10.2138/am-2021-7818. http://www.minsocam.org/

**TABLE 2**. X-ray powder diffraction data (*d* in Å) for celleriite from the Rosina pegmatite, San Piero in Campo, Elba Island, Italy (holotype). Whenever a single box is reported for the $I/I_0$ of a group of nearby reflections, the asterisk, if present, indicates the most intense one(s)

| $I_{meas}$ | $d_{meas}$ | $d_{calc}$ | *hkl* | $I_{meas}$ | $d_{meas}$ | $d_{calc}$ | *hkl* |
|---|---|---|---|---|---|---|---|
| 5 | 7.9771 | 7.9665 | 110 | 38 | **2.0356** | 2.0422 | 223 |
| **45** | **6.3449** | **6.3385** | **101** | **38*** | | **2.0354** | **152** |
| 20 | 4.9462 | 4.9600 | 021 | 8 | 2.0203 | 2.0183 | 161 |
| 13 | 4.6013 | 4.5995 | 030 | 3 | 1.9913 | 1.9916 | 440 |
| **60** | **4.2104** | **4.2106** | **211** | 26 | 1.9130 | 1.9143 | 342 |
| **88** | **3.9826** | **3.9832** | **220** | 5 | 1.9013 | 1.9000 | 701 |
| **55** | **3.4532** | **3.4544** | **012** | 5* | | 1.9000 | 351 |
| 10 | 3.3705 | 3.3726 | 131 | 6 | 1.8663 | 1.8665 | 413 |
| 4 | 3.1047 | 3.1057 | 401 | 7 | 1.8481 | 1.8482 | 621 |
| 10 | 3.0114 | 3.0111 | 410 | 2 | 1.8281 | 1.8276 | 710 |
| **55** | **2.9425** | **2.9448** | **122** | 1 | 1.8122 | 1.8125 | 612 |
| 5 | 2.8940 | 2.8936 | 321 | 5* | 1.7696 | 1.7718 | 333 |
| 5 | 2.6088 | 2.6097 | 312 | 5 | | 1.7693 | 104 |
| **100** | **2.5733** | **2.5739** | **051** | 3* | 1.7258 | 1.7272 | 024 |
| 2 | 2.4801 | 2.4800 | 042 | 3 | | 1.7254 | 072 |
| 2 | 2.4496 | 2.4492 | 241 | 3* | | 1.7254 | 532 |
| 16 | 2.3694 | 2.3786 | 003 | 3 | 1.6873 | 1.6863 | 262 |
| 16* | | 2.3679 | 232 | 17 | 1.6530 | 1.6534 | 603 |
| 17 | 2.3404 | 2.3411 | 511 | 17* | | 1.6534 | 063 |
| 2 | 2.2995 | 2.2997 | 060 | 11 | 1.6404 | 1.6406 | 271 |
| 2 | 2.2095 | 2.2095 | 520 | 13 | 1.5919 | 1.5933 | 550 |
| 11 | 2.1822 | 2.1829 | 502 | 6 | 1.5841 | 1.5846 | 404 |
| 10 | 2.1611 | 2.1618 | 431 | 6 | | 1.5832 | 452 |
| 10 | 2.1088 | 2.1128 | 303 | | | | |
| 10 | | 2.1128 | 033 | | | | |
| 10 | | 2.1053 | 422 | | | | |

This is the peer-reviewed, final accepted version for American Mineralogist, published by the Mineralogical Society of America.
The published version is subject to change. Cite as Authors (Year) Title. American Mineralogist, in press.
DOI: https://doi.org/10.2138/am-2021-7818. http://www.minsocam.org/

**TABLE 3**. X-ray powder diffraction data (*d* in Å) for celleriite from the Pikárec pegmatite, western Moravia, Czech Republic (co-type). Only reflections with $I_{meas} \geq 2$ are reported.

| $I_{meas}$ | $d_{meas}$ | $d_{calc}$ | *hkl* | $I_{meas}$ | $d_{meas}$ | $d_{calc}$ | *hkl* |
|---|---|---|---|---|---|---|---|
| **53** | **6.3264** | **6.3353** | **101** | 18 | 1.6524 | 1.6529 | 063 |
| 20 | 4.9533 | 4.9587 | 021 | 3 | 1.6524 | 1.6529 | 603 |
| 6 | 4.5952 | 4.5999 | 030 | 12 | 1.6402 | 1.6407 | 271 |
| 6 | 4.5952 | 4.5999 | 300 | 14 | 1.5930 | 1.5934 | 550 |
| **54** | **4.2060** | **4.2099** | **211** | 3 | 1.5834 | 1.5838 | 404 |
| **75** | **3.9801** | **3.9836** | **220** | 2 | 1.5827 | 1.5831 | 452 |
| **57** | **3.4497** | **3.4523** | **012** | 4 | 1.5449 | 1.5453 | 461 |
| 7 | 3.3699 | 3.3723 | 131 | 4 | 1.5237 | 1.5241 | 722 |
| 3 | 3.1035 | 3.1056 | 401 | 12 | 1.4972 | 1.4975 | 054 |
| 4 | 3.0094 | 3.0113 | 140 | 2 | 1.4714 | 1.4718 | 244 |
| 4 | 3.0094 | 3.0113 | 410 | 3 | 1.4487 | 1.4490 | 173 |
| **53** | **2.9417** | **2.9435** | **123** | 14 | 1.4470 | 1.4473 | 514 |
| 6 | 2.8918 | 2.8935 | 321 | 5 | 1.4464 | 1.4468 | 642 |
| 4 | 2.6075 | 2.6089 | 312 | 3 | 1.4184 | 1.4187 | 015 |
| **100** | **2.5725** | **2.5739** | **051** | 6 | 1.4174 | 1.4177 | 651 |
| 2 | 2.4480 | 2.4492 | 241 | 3 | 1.4030 | 1.4033 | 633 |
| 7 | 2.3760 | 2.3771 | 003 | 10 | 1.4015 | 1.4018 | 434 |
| 14 | 2.3663 | 2.3674 | 232 | 9 | 1.3546 | 1.3548 | 10.01 |
| 15 | 2.3400 | 2.3411 | 511 | 4 | 1.3402 | 1.3405 | 562 |
| 14 | 2.1816 | 2.1825 | 502 | 3 | 1.3276 | 1.3279 | 660 |
| 9 | 2.1610 | 2.1619 | 431 | 5 | 1.3233 | 1.3236 | 553 |
| 5 | 2.1109 | 2.1118 | 033 | 3 | 1.3220 | 1.3223 | 354 |
| 5 | 2.1109 | 2.1118 | 303 | 2 | 1.3178 | 1.3181 | 045 |
| 4 | 2.1041 | 2.1050 | 422 | 4 | 1.3096 | 1.3098 | 1.10.0 |
| 9 | 2.0405 | 2.0413 | 223 | 4 | 1.3096 | 1.3098 | 10.10 |
| **33** | **2.0343** | **2.0351** | **152** | 2 | 1.3038 | 1.3041 | 832 |
| 7 | 2.0176 | 2.0184 | 161 | 2 | 1.3002 | 1.3004 | 235 |
| 2 | 1.9910 | 1.9918 | 440 | 2 | 1.2756 | 1.2758 | 390 |
| 25 | 1.9134 | 1.9141 | 342 | 2 | 1.2756 | 1.2758 | 930 |
| 3 | 1.8994 | 1.9001 | 351 | 9 | 1.2669 | 1.2671 | 505 |
| 7 | 1.8652 | 1.8658 | 143 | 3 | 1.2548 | 1.2550 | 544 |
| 7 | 1.8476 | 1.8483 | 621 | 4 | 1.2353 | 1.2355 | 0.11.1 |
| 4 | 1.7706 | 1.7712 | 333 | 2 | 1.2073 | 1.2075 | 345 |
| 2 | 1.6857 | 1.6862 | 262 | 3 | 1.1799 | 1.1801 | 11.11 |
| | | | | 6 | 1.1470 | 1.1472 | 10.13 |

**TABLE 4**. Chemical composition for celleriite from the Rosina pegmatite, San Piero in Campo, Elba Island, Italy (holotype) and the Pikárec pegmatite, western Moravia, Czech Republic (co-type)

| Sample | holotype (10 spots) | | co-type |
|---|---|---|---|
| | Average | Range | (single spot) |
| $SiO_2$ wt% | 36.62(23) | 36.19-36.96 | 35.51 |
| $TiO_2$ | 0.09(2) | 0.06-0.14 | - |
| $B_2O_3$ | 10.62[a] | - | 11.61[c] |
| $Al_2O_3$ | 37.08(43) | 36.24-37.64 | 38.57 |
| $FeO_{tot}$ | 1.19(25) | 0.81-1.60 | 3.92 |
| MnO | 10.01(64) | 8.80-11.15 | 6.56 |
| ZnO | - | | 0.30 |
| MgO | 0.06(5) | 0.01-0.09 | - |
| $Na_2O$ | 1.34(16) | 1.04-1.51 | 1.56 |
| $Li_2O$ | 0.42[b] | - | 0.26[c] |
| F | 0.05(4) | 0.00-0.13 | 0.34 |
| $H_2O$ | 3.34[a] | - | 3.10[a] |
| –O = F | –0.02 | | –0.14 |
| FeO | 1.14[d] | | 3.66[d] |
| $Fe_2O_3$ | 0.05[d] | | 0.29[d] |
| Total | 100.79 | | 101.62 |
| **Atomic fractions normalized to 31 anions** | | | |
| Si (apfu) | 5.994 | | 5.754 |
| $Ti^{4+}$ | 0.012 | | - |
| B | 3.000 | | 3.246 |
| Al | 7.154 | | 7.365 |
| $Fe^{3+}$ | 0.007 | | 0.035 |
| $Fe^{2+}$ | 0.156 | | 0.496 |
| $Mn^{2+}$ | 1.388 | | 0.900 |
| Zn | - | | 0.036 |
| Mg | 0.013 | | - |
| Na | 0.424 | | 0.489 |
| Li | 0.277 | | 0.167 |
| F | 0.028 | | 0.174 |
| OH | 3.651 | | 3.350 |

[a] Calculated by stoichiometry.

[b] Determined by μ-LIBS

[c] Determined by LA-ICP-MS.

[d] Determined by Mössbauer spectroscopy.

Errors for oxides and fluorine are standard deviations (in brackets); apfu = atoms per formula unit.

This is the peer-reviewed, final accepted version for American Mineralogist, published by the Mineralogical Society of America.
The published version is subject to change. Cite as Authors (Year) Title. American Mineralogist, in press.
DOI: https://doi.org/10.2138/am-2021-7818. http://www.minsocam.org/

**TABLE 5**. Room temperature $^{57}$Fe Mössbauer parameters for celleriite from the Rosina pegmatite, San Piero in Campo, Elba Island, Italy (holotype) and the Pikárec pegmatite, western Moravia, Czech Republic (co-type)

| δ (mm/s) | $\Delta E_Q$ (mm/s) | Γ (mm/s) | Assignment | Area (%) |
|---|---|---|---|---|
| **holotype** | | | | |
| 1.09 | 2.47 | 0.36 | $^{[6]}Fe^{2+}$ | 81 |
| 1.12 | 2.06 | 0.20 | $^{[6]}Fe^{2+}$ | 6 |
| 1.12 | 1.45 | 0.42 | $^{[6]}Fe^{2+}$ | 9 |
| 0.42 | 0.16 | 0.24 | $^{[6]}Fe^{3+}$ | 4 |
| **co-type** | | | | |
| 1.10 | 2.39 | 0.29 | $^{[6]}Fe^{2+}$ | 41 |
| 1.10 | 2.56 | 0.23 | $^{[6]}Fe^{2+}$ | 26 |
| 1.10 | 1.74 | 0.47 | $^{[6]}Fe^{2+}$ | 25 |
| 1.09 | 1.32 | 0.17 | $^{[6]}Fe^{2.5+}$ | 3 |
| 0.29 | 0.48 | 0.35 | $^{[6]}Fe^{3+}$ | 5 |

*Note*: δ = center shift (with respect to an α-Fe foil); $\Delta E_Q$ = quadrupole splitting; Γ = full width at half maximum ; Area = absorption area. Errors were estimated at about ±0.02 mm/s for δ, $\Delta E_Q$ and Γ, and no less than ±3 % absolute for doublets areas.

This is the peer-reviewed, final accepted version for American Mineralogist, published by the Mineralogical Society of America.
The published version is subject to change. Cite as Authors (Year) Title. American Mineralogist, in press.
DOI: https://doi.org/10.2138/am-2021-7818. http://www.minsocam.org/

**TABLE 6**. Optimized cation site populations (atoms per formula unit), mean atomic numbers and mean bond lengths (Å) for celleriite from the Rosina pegmatite, San Piero in Campo, Elba Island, Italy (holotype) and the Pikárec pegmatite, western Moravia, Czech Republic (co-type)

| | holotype: site population | Mean atomic number | | Mean bond length | |
|---|---|---|---|---|---|
| | | observed | calculated | observed | calculated |
| *X* | 0.58 □ + 0.42 Na | 4.70(8) | 4.68 | | |
| *Y* | 1.10 $Mn^{2+}$ + 0.16 $Fe^{2+}$ + 1.45 Al + 0.01 $Fe^{3+}$ + 0.28 Li + 0.01 $Ti^{4+}$ | 17.11(15) | 17.19 | 2.031 | 2.033[a] |
| *Z* | 5.70 Al + 0.29 $Mn^{2+}$ + 0.01 Mg | 13.47(8) | 13.58 | 1.919 | 1.917[a] |
| *T* | 5.99 Si + 0.01 Al | 14[b] | 14.00 | | |
| *B* | 3 B | 5[b] | 5 | | |
| | co-type: site population | | | | |
| *X* | 0.51 □ + 0.49 Na | 5.36(5) | 5.39 | | |
| *Y* | 0.81 $Mn^{2+}$ + 0.50 $Fe^{2+}$ + 0.04 Zn + 1.46 Al + 0.04 $Fe^{3+}$ + 0.17 Li | 18.11(11) | 18.19 | 2.026 | 2.031[a] |
| *Z* | 5.91 Al + 0.09 $Mn^{2+}$ | 13.10(5) | 13.18 | 1.912 | 1.908[a] |
| *T* | 5.75 Si + 0.25 B | 13.74(5) | 13.63 | | |
| *B* | 3 B | 5[b] | 5 | | |

[a] Calculated from the empirical ionic radii (in Å) of Bosi (2018): Al = 0.547, $Fe^{3+}$ = 0.675, $Fe^{2+}$ = 0.776, $Mn^{2+}$ = 0.809, Zn = 0.740, Li = 0.751, Ti = 0.605; the mean Y and Z anion radii are functions of constituent-anion radius (1.360 and 1.357, respectively).
[b] Fixed in the final stages of refinement.

**TABLE 7** (on deposit). Weighted bond valences (valence units) for celleriite from the Rosina pegmatite, San Piero in Campo, Elba Island, Italy (holotype) and from the Pikárec pegmatite, western Moravia, Czech Republic (co-type)

**holotype**

| Site | *X* | *Y* | *Z* | *T* | *B* | SUM |
|---|---|---|---|---|---|---|
| O(1) | | $0.40^{\times 3}\rightarrow$ | | | | 1.20 |
| O(2) | $0.06^{\times 3}\downarrow$ | $0.47^{\times 2}\downarrow\rightarrow$ | | | 1.04 | 2.03 |
| O(3) | | 0.31 | $0.42^{\times 2}\rightarrow$ | | | 1.16 |
| O(4) | $0.03^{\times 3}\downarrow$ | | | $1.01^{\times 2}\rightarrow$ | | 2.04 |
| O(5) | $0.03^{\times 3}\downarrow$ | | | $0.97^{\times 2}\rightarrow$ | | 1.97 |
| O(6) | | $0.39^{\times 2}\downarrow$ | 0.55 | 1.04 | | 1.99 |
| O(7) | | | 0.53 | 1.04 | | 2.01 |
| O(8) | | | 0.44<br>0.48<br>0.53 | | $0.98^{\times 2}\downarrow$ | 2.00 |
| SUM | 0.36 | 2.44 | 2.96 | 4.06 | 2.99 | |
| MAV[a] | 0.43 | 2.40 | 2.95 | 4.00 | 3.00 | |

**co-type**

| Site | *X* | *Y* | *Z* | *T* | *B* | SUM |
|---|---|---|---|---|---|---|
| O(1) | | $0.42^{\times 3}\rightarrow$ | | | | 1.25 |
| O(2) | $0.07^{\times 3}\downarrow$ | $0.47^{\times 2}\downarrow\rightarrow$ | | | 1.05 | 2.05 |
| O(3) | | 0.31 | $0.42^{\times 2}\rightarrow$ | | | 1.15 |
| O(4) | $0.03^{\times 3}\downarrow$ | | | $0.99^{\times 2}\rightarrow$ | | 2.00 |
| O(5) | $0.04^{\times 3}\downarrow$ | | | $0.95^{\times 2}\rightarrow$ | | 1.95 |
| O(6) | | $0.40^{\times 2}\downarrow$ | 0.56 | 1.02 | | 1.98 |
| O(7) | | | 0.54 | 1.00 | | 1.99 |
| O(8) | | | 0.44<br>0.59<br>0.53 | | $0.97^{\times 2}\downarrow$ | 1.99 |
| SUM | 0.42 | 2.47 | 2.98 | 3.96 | 2.99 | |
| MAV[a] | 0.49 | 2.44 | 2.99 | 3.96 | 3.00 | |

*Note*: Weighted bond valence according to Bosi (2014). Bond-valences obtained from the bond-valence parameters of Gagné and Hawthorne (2015) for cations bonded to $O^{2-}$ and from Brese and O'Keeffe (1991) for cations bonded to $F^{-}$.

[a] Expected mean atomic valence (or formal charge) from the empirical crystal-chemical formula.

This is the peer-reviewed, final accepted version for American Mineralogist, published by the Mineralogical Society of America.
The published version is subject to change. Cite as Authors (Year) Title. American Mineralogist, in press.
DOI: https://doi.org/10.2138/am-2021-7818. http://www.minsocam.org/

**TABLE 8.** Comparative data for the holotype specimens of celleriite, foitite and magnesio-foitite

| | Celleriite[a] | Foitite[b] | Magnesio-foitite[c] |
|---|---|---|---|
| *a* (Å) | 15.9518(4) | 15.967(2) | 15.884(4) |
| *c* | 7.1579(2) | 7.126(1) | 7.178(3) |
| *V* (Å$^3$) | 1577.38(9) | 1573.3(4) | 1568.0(6) |
| Space group | *R*3*m* | *R*3*m* | *R*3*m* |
| Optic sign | Uniaxial (–) | Uniaxial (–) | Uniaxial (–) |
| ω | 1.643(1) | 1.664(1) | 1.650 |
| ε | 1.628(1) | 1.642(1) | 1.624 |
| Streak | White | Greyish-white | Not reported |
| Color | from violet to gray-blue | Bluish black | Pale bluish grey |
| Pleochroism | O = pale violet<br>E = light grey-blue | O = pale lavender<br>E = dark blue | O = grey-blue<br>E = pale lavender |
| Strong lines in the powder XRD pattern *d*(Å) ($I_{meas}$, %) | 2.573 (100)<br>3.983 (88)<br>4.210 (60)<br>3.453 (55)<br>2.943 (55)<br>6.345 (45) | 2.573 (100)<br>3.452 (91)<br>6.338 (84)<br>2.944 (71)<br>4.212 (48)<br>3.989 (38) | 2.567 (100)<br>3.969 (100)<br>4.211 (90)<br>2.949 (70)<br>6.366 (60)<br>3.471 (60) |
| Reference | This work | MacDonald *et al*. (1993) | Hawthorne *et al.* (1999) |

*Note*: The pleochroism reported in MacDonald *et al*. (1993) is anomalous. All other tourmalines reported so far in literature display a reverse pleochroic scheme with O > E.

[a] □$(Mn^{2+}_2Al)Al_6(Si_6O_{18})(BO_3)_3(OH)_3(OH)$

[b] □$(Fe^{2+}_2Al)Al_6(Si_6O_{18})(BO_3)_3(OH)_3(OH)$

[c] □$(Mg_2Al)Al_6(Si_6O_{18})(BO_3)_3(OH)_3(OH)$

Figure 2 (online version)

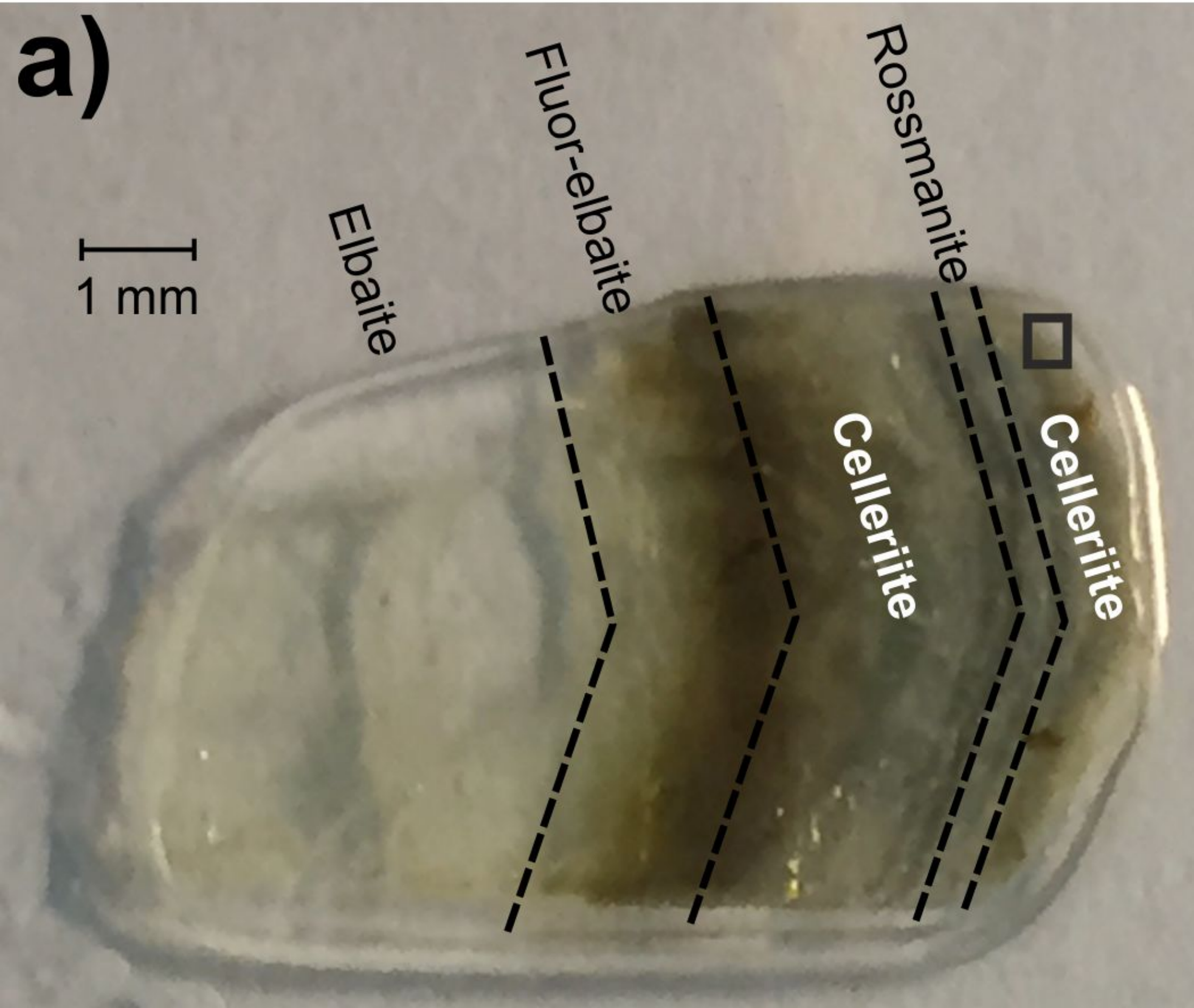

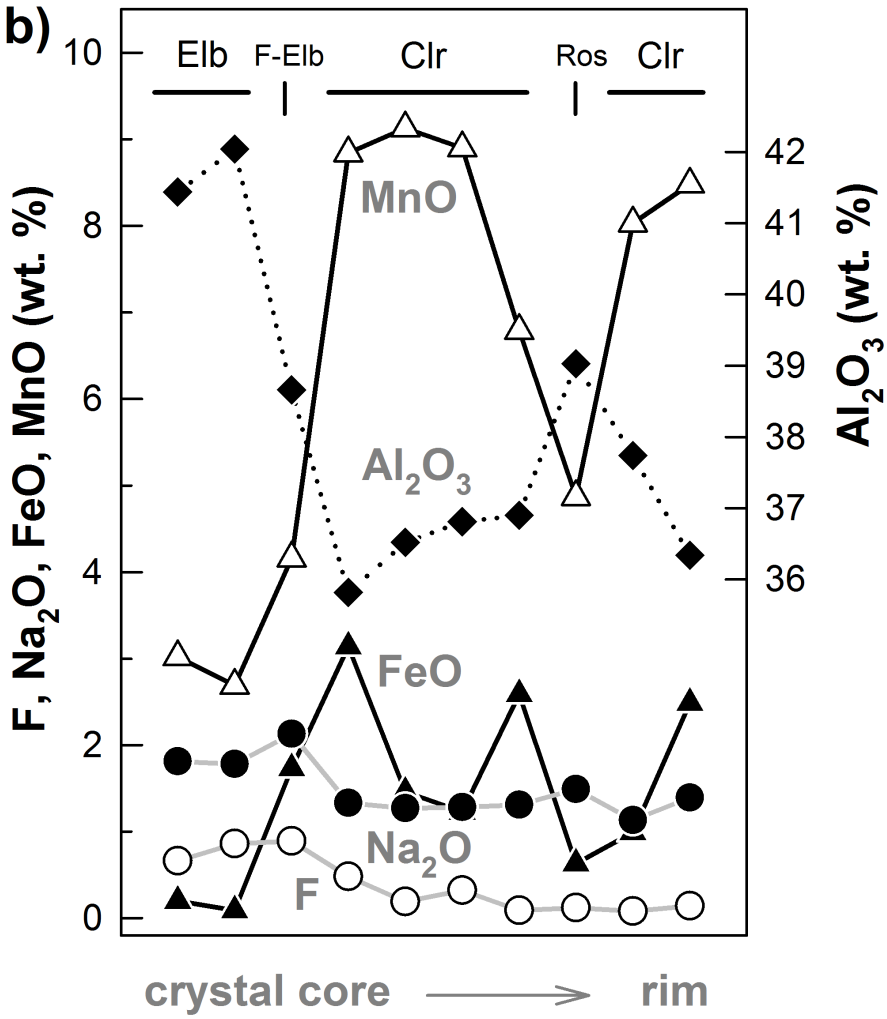
b)
Elb
F-Elb
Clr
Ros
Clr
MnO
Al2O3
FeO
Na2O
F
F, Na2O, FeO, MnO (wt. %)
Al2O3 (wt. %)
crystal core
rim

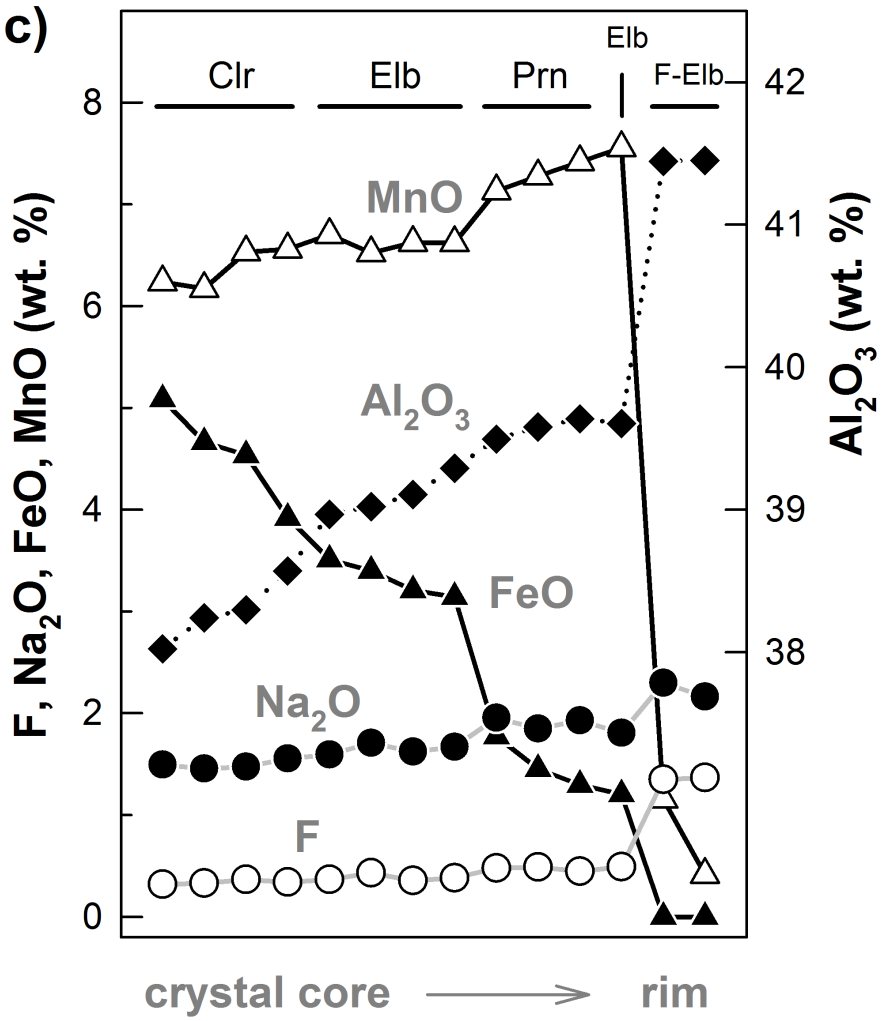
c)
Clr
Elb
Prn
Elb
F-Elb
MnO
Al2O3
FeO
Na2O
F
F, Na2O, FeO, MnO (wt. %)
Al2O3 (wt. %)
crystal core
rim

# Figure 3a (online version)

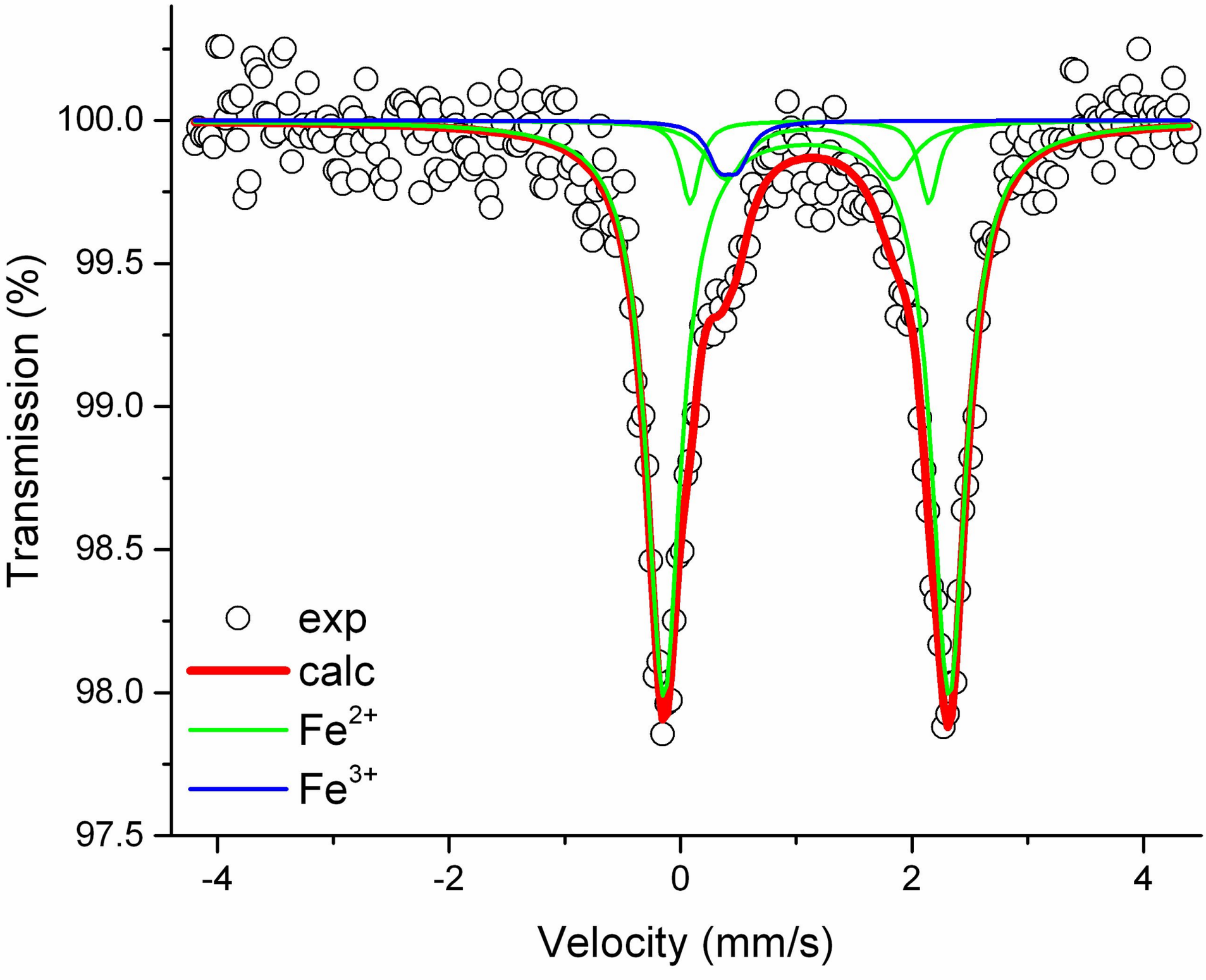

Figure 3b

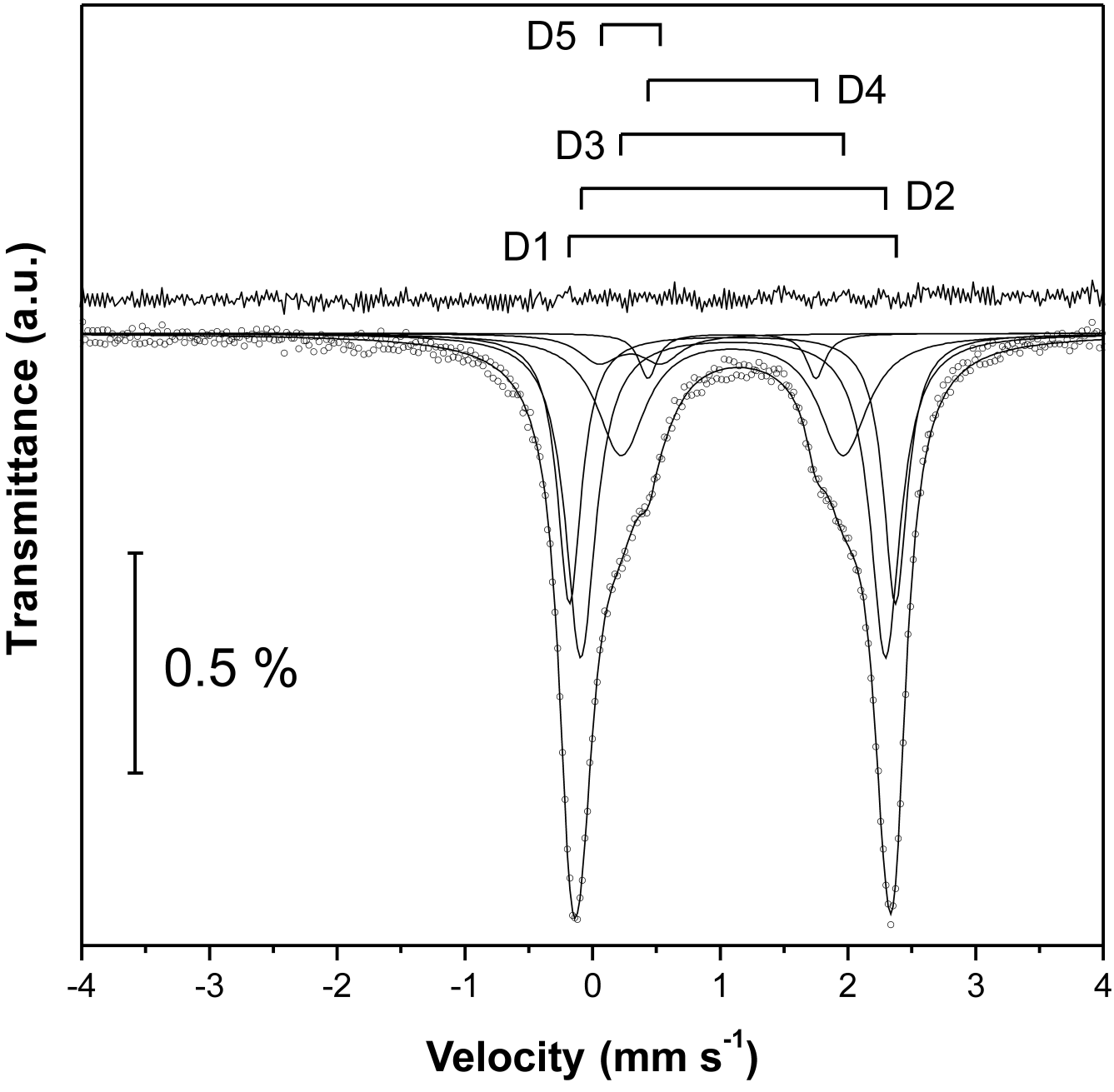

Figure 4

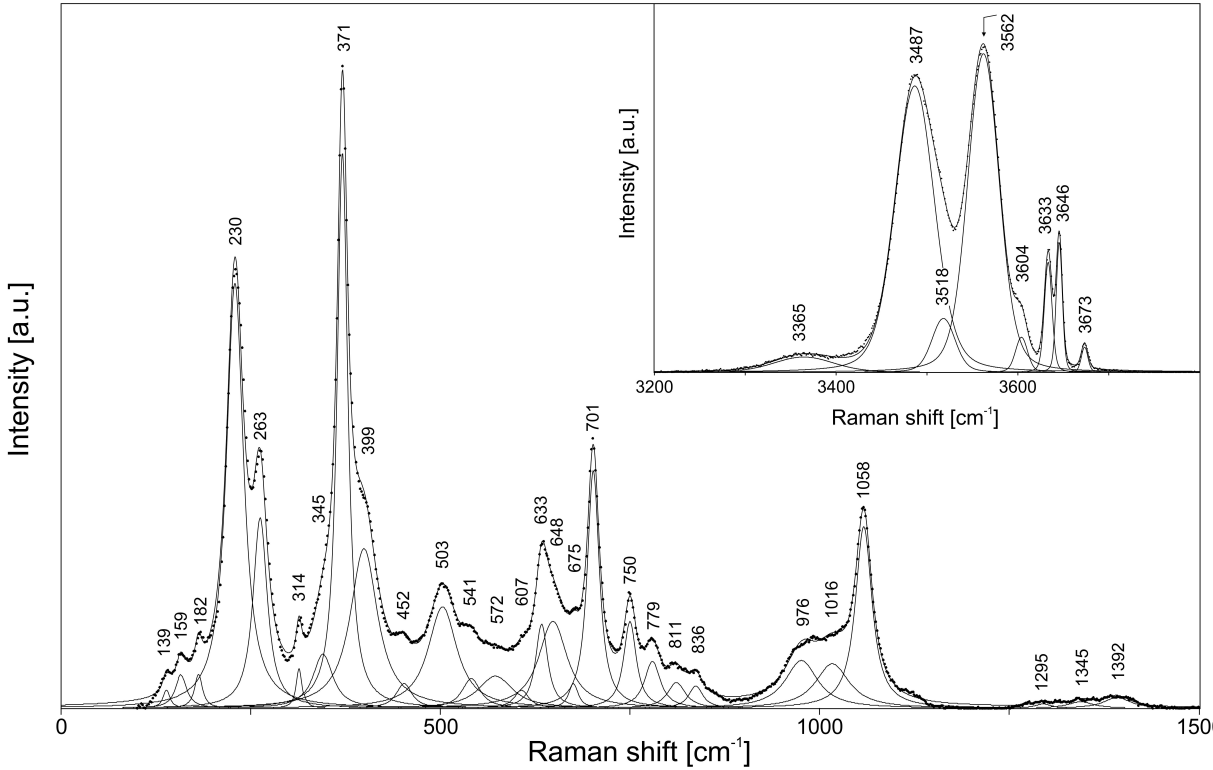
Intensity [a.u.]
Raman shift [cm-1]
0
500
1000
1500
139
159
182
230
263
314
345
371
399
452
503
541
572
607
633
648
675
701
750
779
811
836
976
1016
1058
1295
1345
1392
Intensity [a.u.]
Raman shift [cm-1]
3200
3400
3600
3365
3487
3518
3562
3604
3633
3646
3673

Figure 5

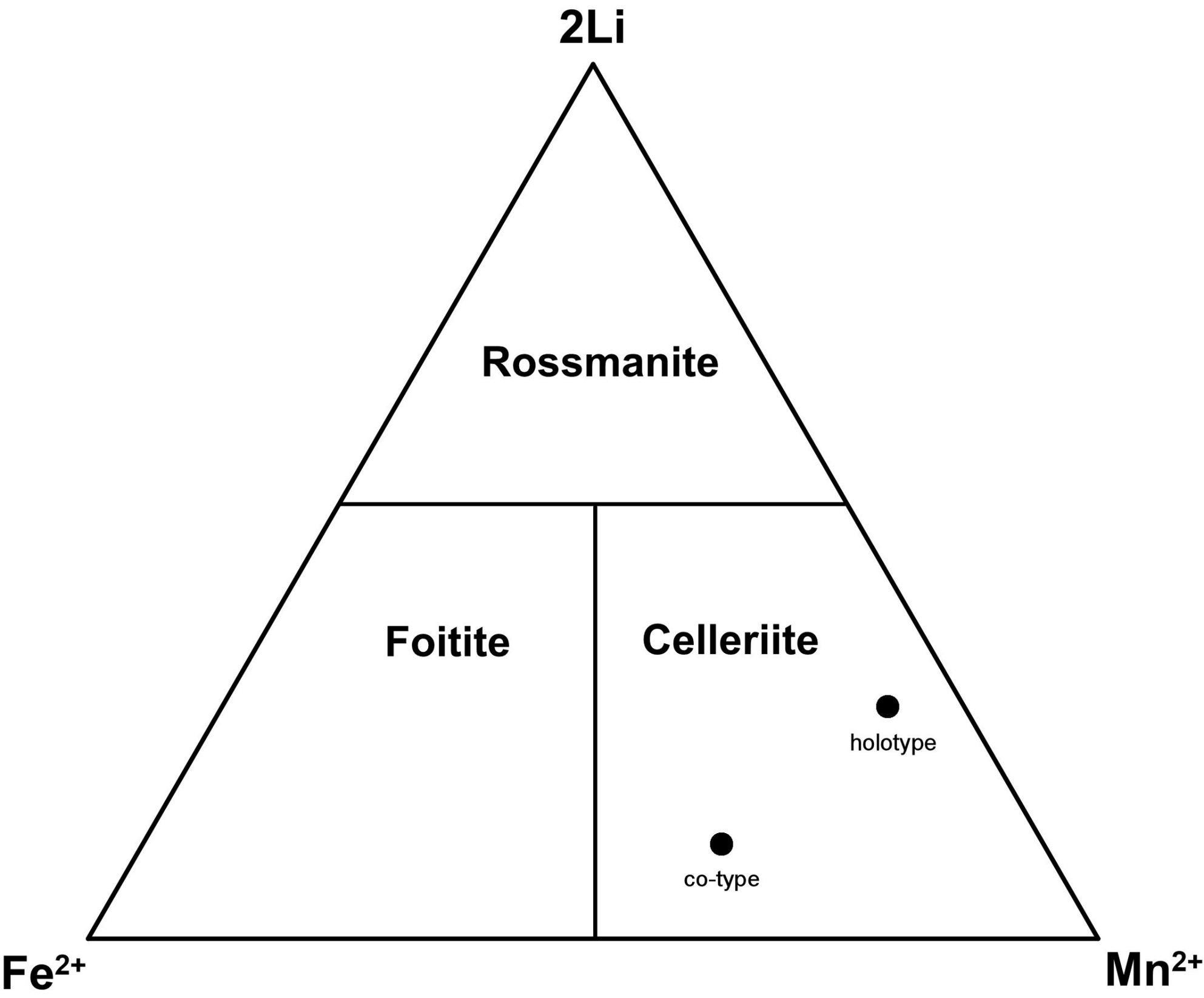
2Li
Rossmanite
Foitite
Celleriite
holotype
co-type
Fe2+
Mn2+